








Contourite characterization and its discrimination from other deep-water deposits in the Gulf of Cadiz contourite depositional system

SANDRA DE CASTRO* , FRANCISCO JAVIER HERNÁNDEZ-MOLINA* ,
WOUTER DE WEGER* , FRANCISCO JOSÉ JIMÉNEZ-ESPEJO† ,
FRANCISCO JAVIER RODRÍGUEZ-TOVAR‡, ANXO MENA§ ,
ESTEFANÍA LLAVE¶  and FRANCISCO JAVIER SIERRO** 

*Department of Earth Sciences, Royal Holloway Univ. London, Egham, Surrey TW20 0EX, UK
(E-mail: Sandra.deCastroSantos.2017@live.rhul.ac.uk)

†Instituto Andaluz de Ciencias de la Tierra (CSIC-IACT), Granada 18100, Spain

‡Departamento de Estratigrafía y Paleontología, Universidad de Granada, Granada 18002, Spain

§Departamento de Xeociencias Mariñas e Ordenación do Territorio, University of Vigo, Vigo 36310, Spain

¶Instituto Geológico y Minero de España (IGME), Madrid 28003, Spain

**Departamento de Geología, Universidad de Salamanca, Plaza de los Caídos, Salamanca 37008, Spain

Associate Editor – Adam McArthur

ABSTRACT

Despite numerous efforts to properly differentiate between contourites and other deep-water deposits in cores and outcrops, reliable diagnostic criteria are still lacking. The co-occurrence of downslope and along-slope sedimentary processes makes it particularly difficult to differentiate these relatively homogeneous deposits. The main aim of this paper is to identify differences in deep-water sediments based on Principal Component Analysis of grain size and geochemistry, sedimentary facies, and reinforced by microfacies and ichnofacies. The sediments studied were obtained from two International Ocean Drilling Program Expedition 339 sites in mounded and sheeted drifts in the Gulf of Cadiz. The statistical approach led to the discernment of hemipelagites, silty contourites, sandy contourites, bottom current reworked sands, fine-grained turbidites and debrites over a range of depositional and physiographic elements. These elements are linked to contourite drifts, the drift-channel transition, the contourite channel and distal upper slope. When bottom currents or gravity-driven flows are not the dominant depositional process, marine productivity and continental input settling forms the main depositional mechanism in deep-water environments. This is reflected by a high variability of the first principal component in hemipelagic deposits. The stacked principal component variability of these deposits evidences that the contourite drift and the adjacent contourite channel were influenced by the interrelation of hemipelagic, gravitational and bottom current induced depositional processes. This interrelation questions the paradigm that a drift is made up solely of muddy sediments. The interrelation of sedimentary processes is a consequence of the precession-driven changes in the intensity of the Mediterranean Outflow Water related to Mediterranean climate variability, which are punctuated by millennial-scale variability. Associated vertical and lateral shifts of the Mediterranean Outflow Water, and therefore of its interface with the East North Atlantic Central Water, controlled sediment input and favoured turbulent sediment transport in the middle slope. During

the interglacial precession maxima/insolation minima, a more vigorous upper core of the Mediterranean Outflow Water and the enhanced impact of the East North Atlantic Central Water – Mediterranean Outflow Water interface allowed for the development of the sandier contourite deposits.

Keywords Contourites, deep-water processes, Gulf of Cadiz, hemipelagites, mixed-systems, turbidites.

INTRODUCTION

The pioneering study on deep-water mass circulation is from Wüst (1936). Decades later, direct evidence of the action of bottom currents was obtained through photographs of the seafloor (Heezen *et al.*, 1954; Heezen *et al.*, 1959; Pettijohn & Potter, 1964; Dzulynski & Walton, 1965; Heezen & Hollister, 1971). Since then, there has been an exponential boom in deep-marine research and the characterization of bottom current deposits, yet considerable controversy still exists when discerning contourites from turbidites and hemipelagic deposits.

A commonly accepted paradigm holds that deep-marine environments, if not affected by gravitational processes, are predominantly made up of very fine-grained sediment (Stow & Lovell, 1979; Gonthier *et al.*, 1984; Stow & Piper, 1984). Thus, deep-marine environments feature currents and oceanographic processes that may be energetic, can alter the morphology of the seafloor and may even form coarse-grained sandy deposits (McCave & Tucholke, 1986; Viana *et al.*, 1998; Rebesco *et al.*, 2014). Indeed, changes in the hydrodynamic characteristics of bottom currents may repeatedly shift between bedload-dominated and suspension-load-dominated deposition, with episodes of erosion, winnowing and reworking (McCave, 2008; Stow *et al.*, 2008; Hüneke *et al.*, 2020).

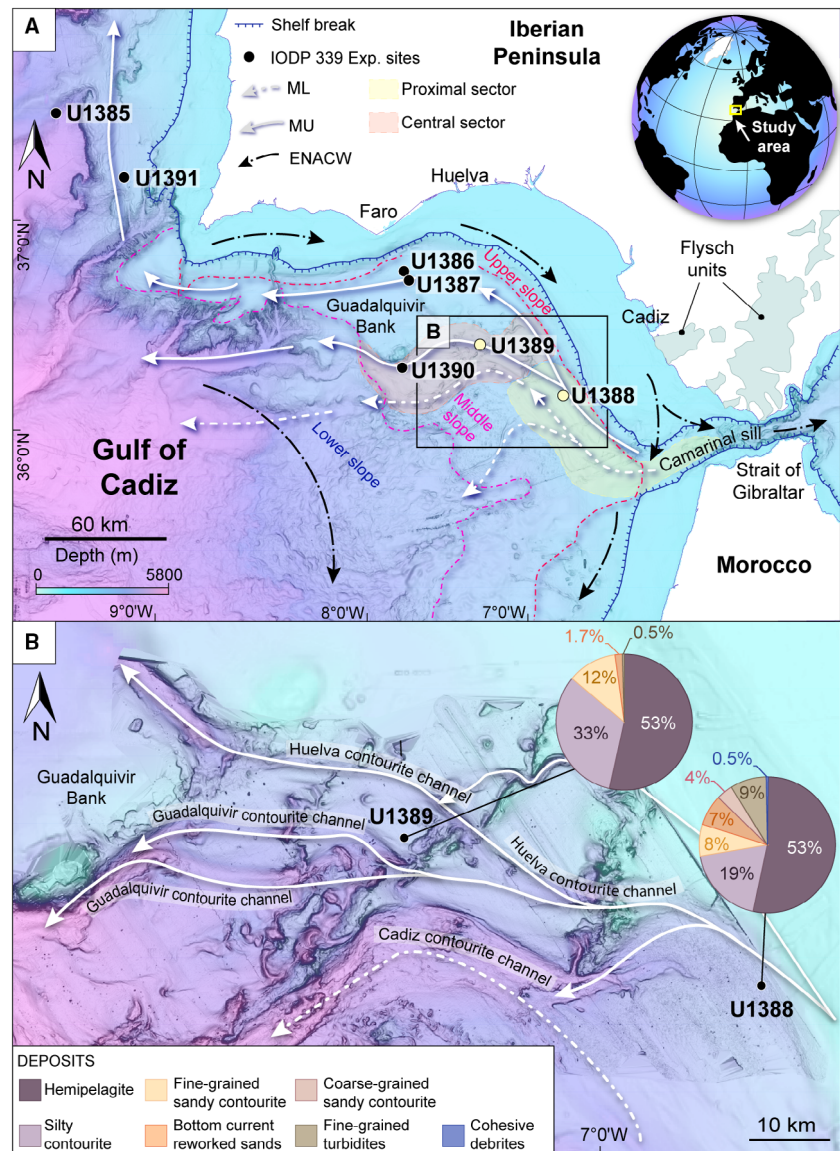
The criteria used to distinguish between contouritic, turbiditic and hemipelagic deposits, especially in the fossil record, have been the subject of a debate that continues to the present day. The co-occurrence of biogenic and terrigenous sediment settling plus downslope and along-slope sedimentary processes makes it particularly hard to differentiate. In the context of contourites, two different concepts have been proposed for interpretation. The first bases the diagnosis of contourites on the presence and abundance of bioturbation (Lovell & Stow, 1981; Stow, 1982; Gonthier *et al.*, 1984). The second argues that primary sedimentary structures

should be the basic criterion for contourite recognition (Shanmugam *et al.*, 1993a,b; Shanmugam, 2000; Martín-Chivelet *et al.*, 2008). The coexistence or intermittence of deep-marine sedimentary processes responsible for the formation of these deposits needs to be further explored, and the controlling factors evaluated.

The interest in distinguishing among contourites, turbidites and hemipelagites based on: (i) the role of mixed turbiditic–contouritic systems in deep-water petroleum plays (Sansom, 2018; Fonnesu *et al.*, 2020); (ii) implications for mineral resources and for the judicial determination of a continental shelf's outer limits since contourites shape continental shelf morphology (Rebesco *et al.*, 2014; Mosher *et al.*, 2017); (iii) the environmental impact of bottom current deposits in the accumulation of microplastics (Courtene-Jones *et al.*, 2019; Kane *et al.*, 2020); (iv) the close link between contourites and deep-water ecosystems (Hebbeln *et al.*, 2016; Lüdmann *et al.*, 2016; Lozano *et al.*, 2020); and (v) slope stability and other geohazards (Laberg & Camerlenghi, 2008; Miramontes *et al.*, 2018). Despite this interest, there is still no clear criteria for contourite characterization and its discrimination from other deep-water deposits.

The geological setting of the Gulf of Cadiz continental margin is influenced by the Mediterranean Outflow Water (MOW) along the middle slope (Maldonado *et al.*, 1999), giving rise to the interaction of hemipelagic, along-slope and downslope sedimentary processes. This work documents the nature of closely interbedded contouritic, turbiditic and hemipelagic deposits within contourite drift successions in the proximal and central sectors of the Gulf of Cadiz through the study of two sites drilled in the middle slope during the International Ocean Drilling Program (IODP) Expedition 339 (Fig. 1). Three main objectives are pursued in the present work: (i) the sediment facies interpretation as the diagnostic criteria used to discriminate contourites from other deep-water deposits; (ii) characterization of the diversity of lateral and

Fig. 1. (A) Gulf of Cadiz showing the pathway of Mediterranean Outflow Water (MOW; MU = upper core in continuous white arrows; and ML = lower core in dashed white arrows) after it exits the Gibraltar Gateway; and Eastern North Atlantic Central Water (ENACW; black arrows) inflow towards the Mediterranean Sea (adapted from Hernández-Molina *et al.*, 2014; Sánchez-Leal *et al.*, 2017). International Ocean Drilling Program (IODP) Expedition 339 site locations are indicated by black dots, and the U1388 and U1389 (in the proximal and central sectors, respectively) are indicated by pale yellow dots. (B) Circulation of the MU and ML along the Gulf of Cadiz middle slope with the present day interplay of morphological features generated by along-slope and downslope processes. Pie chart for the main deposit percentages at each site are included. MU; Mediterranean Upper, ML; Mediterranean Lower.



vertical associations of hemipelagites, turbidites and fine-grained and coarse-grained contourites in view of their sedimentary texture and geochemical signals in the study area; and (iii) establishment of the controlling factors behind deposition of these deep-marine deposits and how they contribute to overall drift construction.

MORPHOSEDIMENTARY AND OCEANOGRAPHIC FRAMEWORK

The northern continental margin of the Gulf of Cadiz runs from the Strait of Gibraltar to the south-west tip of Portugal (Fig. 1A). Along the

middle slope, between 400 to 500 m and 1200 m water depth, a large contourite depositional system (CDS) has developed since the early Pliocene (Faugères *et al.*, 1984; Nelson *et al.*, 1999; Llave *et al.*, 2001, 2007, 2019; Hernández-Molina *et al.*, 2003, 2006, 2016). This CDS comprises five major morphosedimentary sectors, with erosional elements prevailing close to the Strait of Gibraltar transitioning towards depositional features found distally and northward (Llave *et al.*, 2001, 2007; Hernández-Molina *et al.*, 2003). This study focuses on the proximal and central sectors, respectively, at Sites U1388 and U1389 of IODP Expedition 339 (Fig. 1A). Site U1388 lies in the proximal scour and sand ribbon sector near the Strait of

Gibraltar, which consists of a thick (*ca* 815 m) sandy sheeted drift (Buitrago *et al.*, 2001; Stow *et al.*, 2013a; Hernández-Molina *et al.*, 2016). Site U1389 is in the channel and ridge sector of the relative topographic high of the Huelva mounded drift (Stow *et al.*, 2013a; Hernández-Molina *et al.*, 2016). The drift is currently elevated 50 to 250 m above the adjacent contourite channels (Figs 1 and 2A). This central sector hosts depositional and erosional contouritic features that interact with marginal valleys (García *et al.*, 2009; Lozano *et al.*, 2020).

The hydrodynamic setting is dominated by the exchange of Atlantic and Mediterranean water masses across the Strait of Gibraltar (Ochoa & Bray, 1991; Bryden *et al.*, 1994). This strait acts as a confined gateway that allows flow of the North Atlantic Surficial Water (NASW) between 0 m and 100 m water depth, and the Eastern North Atlantic Central Water (ENACW) between 100 m and 300 m water depth (Bellanco & Sánchez-Leal, 2016) into the Mediterranean (Fig. 2), overriding the warm and highly saline MOW flowing into the Atlantic. After exiting the Strait of Gibraltar, the MOW moves in a north-westward direction along the middle slope at water depths between 300 m and 1200 m (Fig. 1A). The Mediterranean upper water (MU) flows at depths between 300 m and 800 m along the base of the upper slope, while the Mediterranean lower water (ML) flows at depths between 800 m and 1200 m (Figs 1 and 2). The MU constitutes the most relevant water mass in the upper to middle slope transition and flows with an average velocity of 0.4 to 0.5 m s⁻¹ (Sánchez-Leal *et al.*, 2017).

DATASET AND METHODS

Core data and age model

The studied cores were collected from IODP Expedition 339 Sites U1388 and U1389

(Expedition 339 Scientists, 2012; Hernández-Molina *et al.*, 2013; Stow *et al.*, 2013b) (Table 1; Fig. 1). Sedimentary analysis focused on cores from Holes U1389A (0 to 390 metres composite depth, mcd) and U1388B (0 to 225 mcd). Sedimentary facies and facies associations were interpreted by means of high-resolution core imaging according to colour, bed boundaries, sedimentary structures, ichnological features, microfacies and major geochemical elements. This study uses the age model published by Sierro *et al.* (2020) and six ¹⁴C dates from the upper part (Bahr *et al.*, 2015) for Site U1389.

Textural analysis

Grain-size analysis was conducted at 25 cm sampling intervals, resulting in 512 samples with a total length of 106.5 m from Site U1388B and 1316 samples with a total length of 335.5 m from Site U1389A. Analysis was performed on bulk sediment using a Malvern Mastersizer S laser microgranulometer (Malvern Panalytical, Malvern, UK; EPOC, University of Bordeaux, France), ranging from 0.02 to 2000 µm (clay to sand). Grain-size parameters were obtained using Gradistat software (Blott & Pye, 2001). The D50, standard deviation, skewness and kurtosis were calculated using a geometric graphical method after Folk & Ward (1957) and Martins (2003).

Major geochemical elements

Major elements were measured by X-ray fluorescence (XRF) scanning that spanned a total length of 106.5 m at Site U1388B and 335.5 m at Site U1389A (Table 1). The XRF core data were collected at 3 cm intervals using a XRF Core Scanner II (Avaatech Serial No. 2; Avaatech B.V., Dodewaard, The Netherlands) in the MARUM laboratories of the University of Bremen (Germany). Further technical details about the XRF equipment, data acquisition and processing can be found in de Castro *et al.* (2020).

Fig. 2. Oceanographic circulation showing the projected conductivity, temperature and depth (CTD) observations collected in the proximal sector (U1388) for temperature (A) and salinity (B); and in the central sector (U1389) for temperature (C) and salinity (D) from the WODB, WOCE, MEDATLAS, Coriolis and SeaDataNet databases, complemented by data from individual cruises carried out by the University of Cádiz (Golfo, 2001TS3; Medout, 2011TS4; Estrecho, 30 2008TS5). Below the surface layer, the 36.3 isohaline approximately defines the interface between ENACW (with salinities down to 36.0) and Mediterranean Outflow Water (MOW) >38.25 (Sánchez-Leal *et al.*, 2017). Note that the proximal domain along the middle slope is clearly dominated by the influence of the upper core of the MOW. ENACW, Eastern North Atlantic Central water; NASW, Northern Atlantic Surface Water; MU, Mediterranean Upper core.

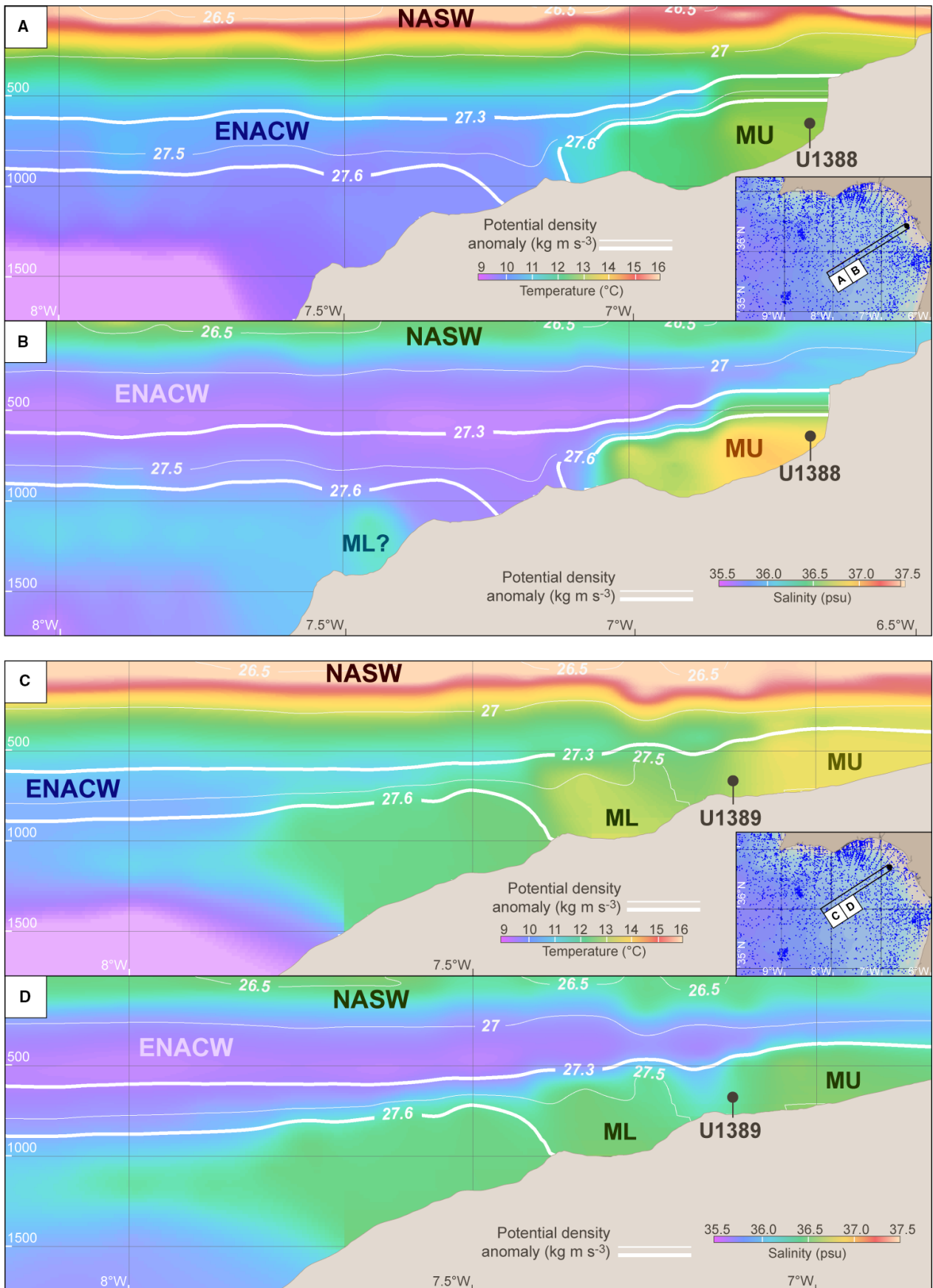


Table 1. Sites U1388 and U1389 core summary (Expedition 339 Scientists, 2012)

Site	Longitude/ Latitude	Water depth (m bsl)	Holes retrieved	Studied holes	Hole recovery (%)	Core length (m)	XRF scan analysis (m)	Grain size	Thin sections	Age model (kyr)
U1388	36°16.142'N/ 6°47.648'W	663	A, B, C	B	47.2	225.7	106.5	512	3	–
U1389	36°25.515'N/ 7°16.683'W	644	A, B, C, D, E	A	94.0	357.0	335.5	1316	37	485

Sites U1388B and U1389A were analyzed in 2016 with generator settings of 10 kV and 30 kV, respectively, at 0.4 mA and 1.0 mA. Sampling time was 20 s at the split core surface. Site U1389A was re-analyzed in 2017 with generator settings of 10 kV and 30 kV at 0.2 mA and 0.75 mA, respectively, and a sampling time of 10 s. Areas of coarse-grained sediment with shell fragments (debrites) were not scanned. Data were retained only from elements that gave a consistently good signal quality (Al, Si, K, Ca, Ti, Br, S, Fe, Sr and Zr). These elements were standardized according to mean values and standard deviations at each site for the different years in which measurements were conducted. Usually elements are normalized to Al, but because this element is at the limit of Avaatech measurement, an alternative element divisor characteristic of the detrital phase was used (K or Ti) (Tjallingii *et al.*, 2007).

Statistical analysis

Pearson correlation coefficients were calculated at Sites U1388 and U1389 to identify significant relationships and element associations. To investigate the different factors influencing the geochemical composition and grain size of the sediment, and to distinguish between sedimentary processes, Principal Component Analysis (PCA) was used in conjunction with PAST 4.0 software (Hammer *et al.*, 2001): PCA is a well-established dimension-reducing statistical technique, applied for pattern recognition in multivariate datasets (Wold *et al.*, 1987; Zou *et al.*, 2006; Abdi & Williams, 2010). The calculated eigenvalues give a measure of the variance accounted for by the corresponding components (axes of the PCA). Principal components (PCs) with eigenvalues of <8.0 were excluded from the interpretation as they represent minor variance.

The PCA was performed on the major elements and all particle sizes (clay to very coarse-grained sand), which were combined in a single array of samples (Site U1388 $n = 512$ and Site U1389 $n = 1316$) for each variable and core depth.

Thin sections

Forty thin sections (4×1 cm) were prepared at Royal Holloway University of London (RHUL, UK) to document microfacies and small-scale sedimentary structures. Modal analysis was conducted by Blackburn Geoconsulting (Bo'ness, UK) on 14 samples and on 26 samples at RHUL. Modal and petrographic analysis were used to determine the composition of 300 points for each thin section by means of a stepping stage. The proportions of components provided in Table S1 were re-normalized to 100%.

Ichnological analysis

Ichnological analysis of core samples was conducted after digital enhancement of high-resolution images to increase visibility of biogenic structures. This procedure is described in Dorador *et al.* (2014a,b) and Dorador & Rodríguez-Tovar (2018). Orientation, shape, size, distribution, infilling material and degree of bioturbation were recorded.

Nomenclature

For this study, the nomenclature for contourites after Faugères & Stow (2008) and Rebesco *et al.* (2014) was adapted. The classification of clastic contourite deposits as silty (4 to 63 μm) and sandy contourites (63 to 2000 μm) is based on Rebesco *et al.* (2014) and Brackenridge *et al.* (2018). Hemipelagic deposits follow the definitions and criteria from Hesse (1975), O'Brien

Table 2. Types of the seven facies differentiated by physical, geochemical and ichnological character, as well as their interpretation in terms of sedimentary processes. BCRS, bottom current reworked sands. The asterisk in F7 represents that X-ray fluorescence (XRF) measurements were made in the matrix of the bioclastic conglomerate

	F1	F2	F3	F4	F5	F6	F7
Texture	Massive	Mottled	Mottled/patchy	Heterolithic/ rippled	Massive	Normal-graded	Chaotic
Bioturbation	Scarce	Moderate	High	Scarce	Scarce/absent	Scarce	Scarce/ absent
Grain size	Fine silt	Fine silt	Medium silt to very fine sand	Fine sand	Medium sand	Medium silt to very fine sand	Fine to coarse sand
Sorting	Poorly sorted	Very poorly sorted	Very to poorly sorted	Poorly to moderately sorted	Well-sorted	Very poorly sorted	Very poorly sorted
PC1	High positive	Next to zero	Negative (contourite). Positive (turbidite)	High negative	High negative	High positive	High positive*
PC2	Negative or next to zero	Positive or next to zero	High positive	High positive	High positive	High positive	High positive*
PC3	Negative or next to zero	Positive or next to zero	Positive	High positive	High positive	Negative	Negative*
Br/Ti	Low	Low	High (contourite). Low (turbidite)	High	High	Low	Low*
Ti/Ca	High	Low	Low	Low	Low	High	High*
Zr/Ti	Low	Transitional	High	High	High	Low	Low*
Sr/Ca	Low	Low	Transitional to high	Low	High	High	High*
Si/K	Low	Low	High	High	High	Low	Low
Interpretation	Hemipelagic	Silty contourite	Fine-grained sandy contourite	BCRS	Coarse-grained sandy contourite	Fine-grained turbidite	Cohesive debrite

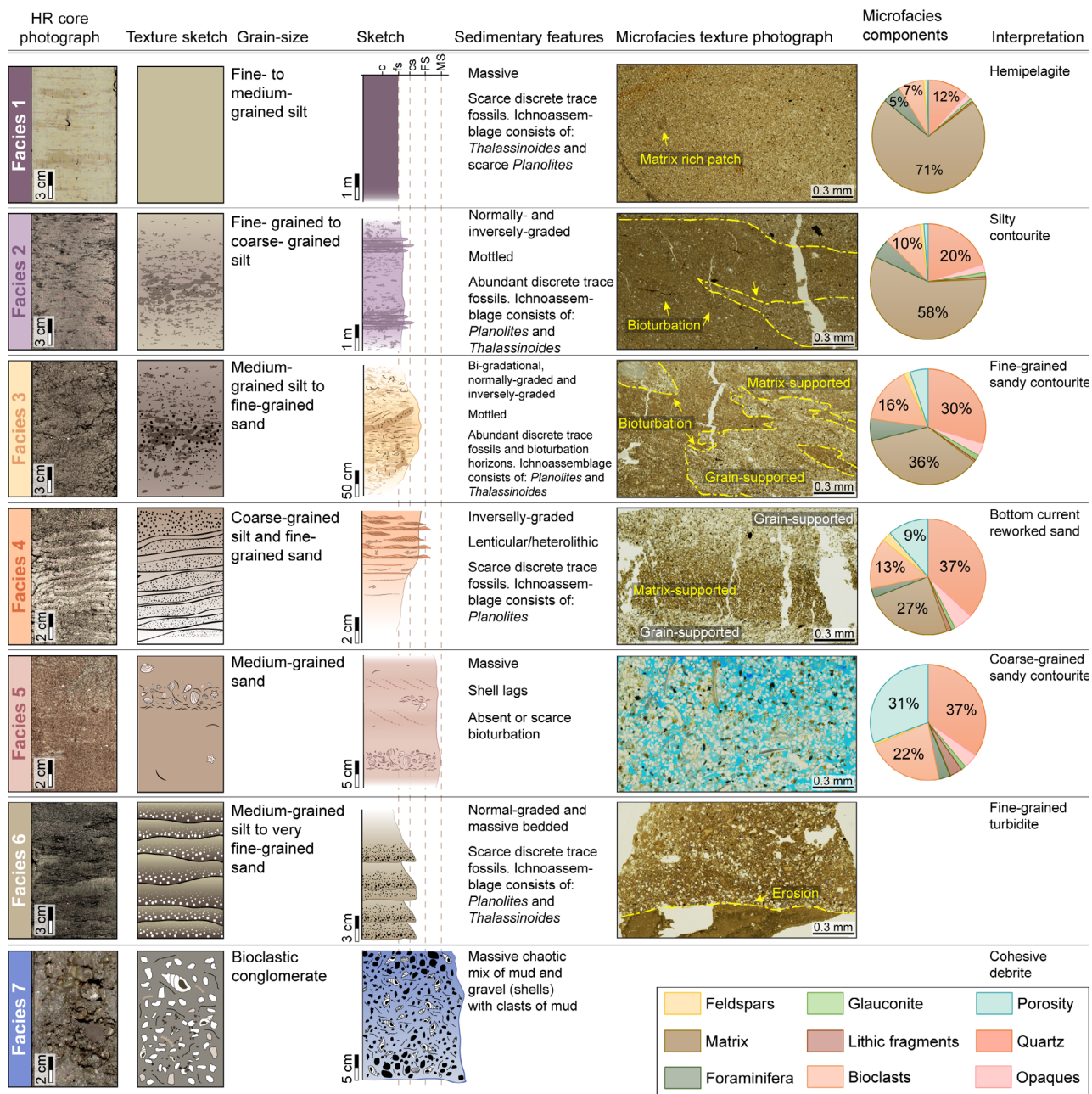


Fig. 3. Summary of the main characteristics of the seven facies (F1 to F7) identified in this work. Microfacies images were taken with plane polarized light (PPL).

et al. (1980) and Stow & Tabrez (1998); fine-grained turbidites are based on Middleton & Hampton (1973), Lowe, (1982) and Stow & Piper (1984). Bottom current reworked sands are based on the definitions from Shanmugam et al. (1993a,b) and cohesive debris-flow deposits (debrites) based on criteria from Middleton & Hampton (1973) and Lowe (1979).

RESULTS

Sedimentary facies description

Seven facies were identified based on their sedimentary, ichnological and petrological characteristics (Table 2).

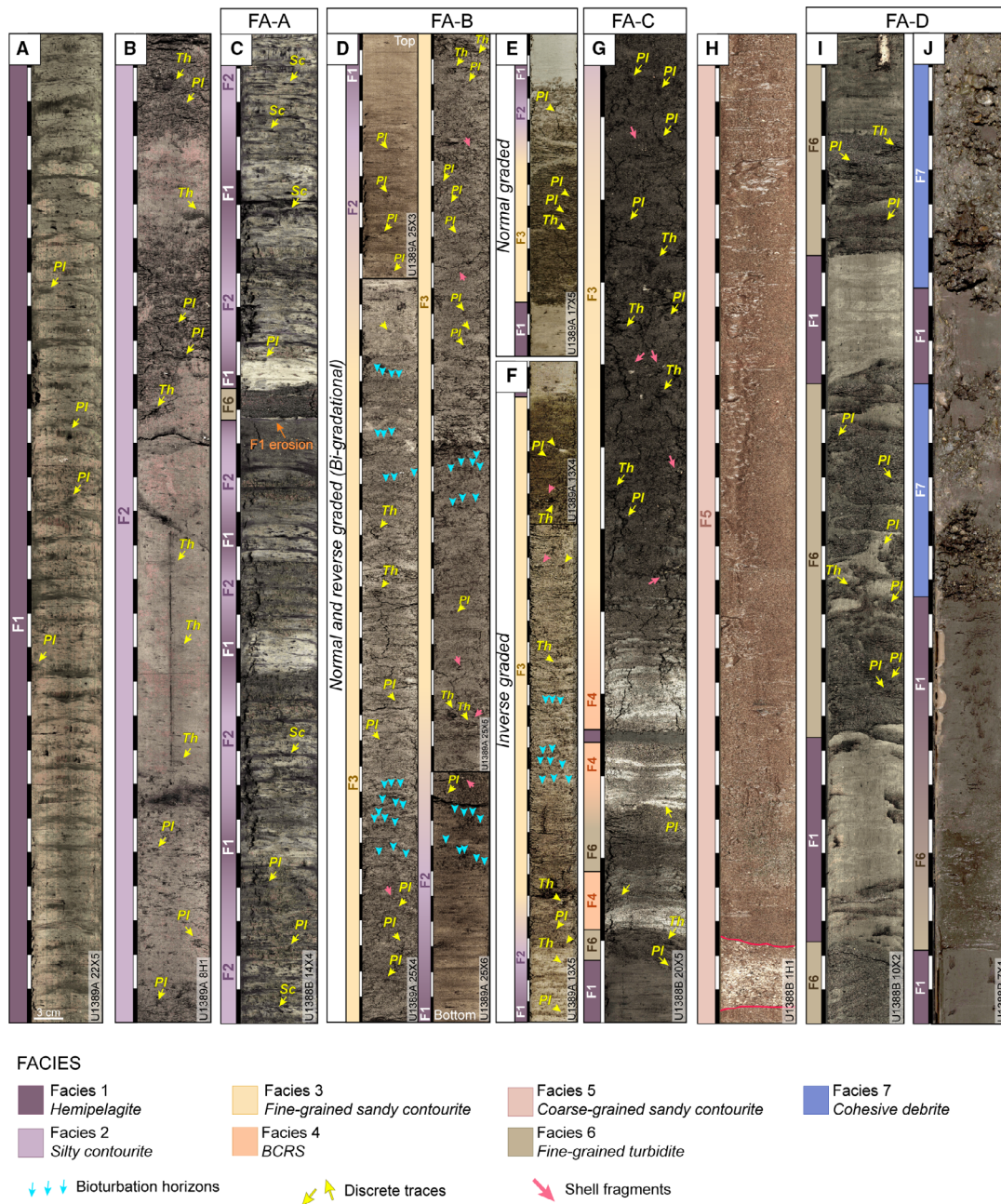


Fig. 4. High-resolution core images of the sedimentary sequences showing sedimentary facies, vertical facies associations, trace fossils and bioturbation horizons. (A) Facies 1 (F1), massive fine-grained to medium-grained silt characterized by locally discrete trace fossils (*Planolites*, *Pl*). The darker layers in F1 receive the name *gravy* and are an effect of the extended core barrel (XCB) drilling method. (B) Facies 2 (F2) mottled fine-grained silt and medium-grained to coarse-grained silt. Note the fine-grained intervals with fine-grained filled traces (?*Planolites* and *Scolicia*, *Sc*), but without coarse infilled traces. The coarser beds show a gradational base and top and are totally bioturbated (*Planolites* and *Thalassinoides*, *Th*). (C) Facies alternation between F1 and F2 (Facies Association A). (D) Normal and inverse graded (bi-gradational) Facies Association B. The high-resolution core images are contiguous downcore from the top (U1389A 25X3) to the bottom (U1389A 25X6). Note the highly bioturbated F3 interval which alternates between discrete traces (*Planolites* and *Thalassinoides*) and bioturbation horizons. BCRS, bottom current reworked sands. Normal-graded (E) and inverse-graded (F) Facies Association B. (G) Facies Association C. (H) Massive Facies 5 (F5) medium-grained sands, without differentiated traces. Note the presence of coarse-shell lags at the base of the section (red lines). (I) Facies association D with Facies 6 (F6) intercalations and (J) Facies association D with F6 and Facies 7 (F7) intercalations. Several unfragmented gastropods are present in F7, and irregular pockets/clasts of mud occur.

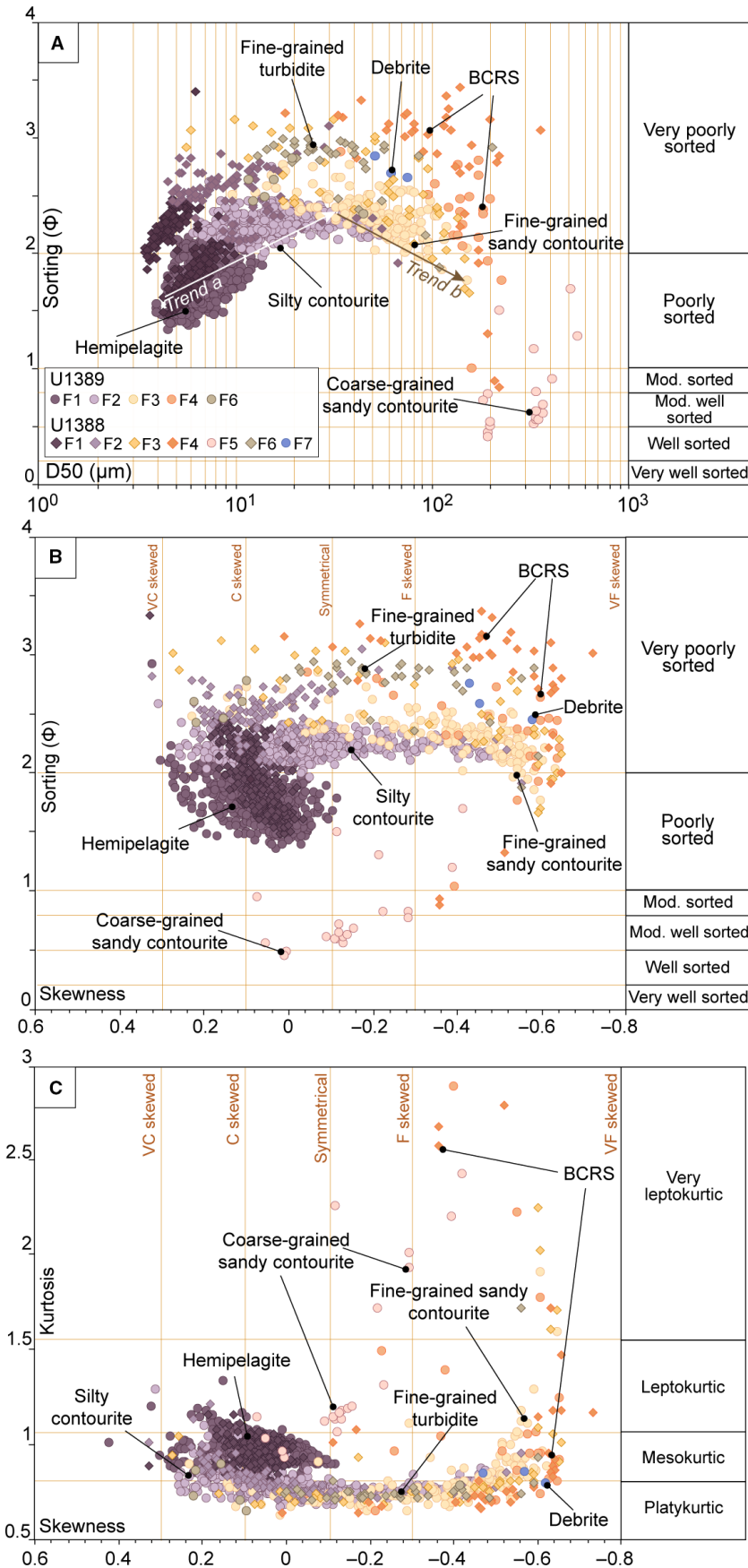


Fig. 5. Facies and grain-size parameters. (A) Cross-plot of sorting (Φ) against D50 showing a second trend in Site U1388 representing sediment input from a different source, which decreases the sorting efficiency. This cross-plot shows that F1 and F2 are characterized by a general decrease in sediment sorting with increasing mean grain size (trend a), whereas the opposite holds for F3 to F4 (trend b). Although the sites provide evidence for these distinct trends, some samples from Site U1388 emphasize a divergence to a characteristic parallel trend of less-sorted sediments from F1 to F4. The best-sorted sands are from certain samples of F4 and F5; and the coarse-grained sandy contourites associated with dune facies (F5) are totally isolated from the rest of the dataset. (B) Sorting versus skewness likewise presents the second trend in Site U1388. (C) Kurtosis versus skewness. The difference in colours between U1388 and U1389 highlights the distinctive trends between sites. BCRS, bottom current reworked sands.

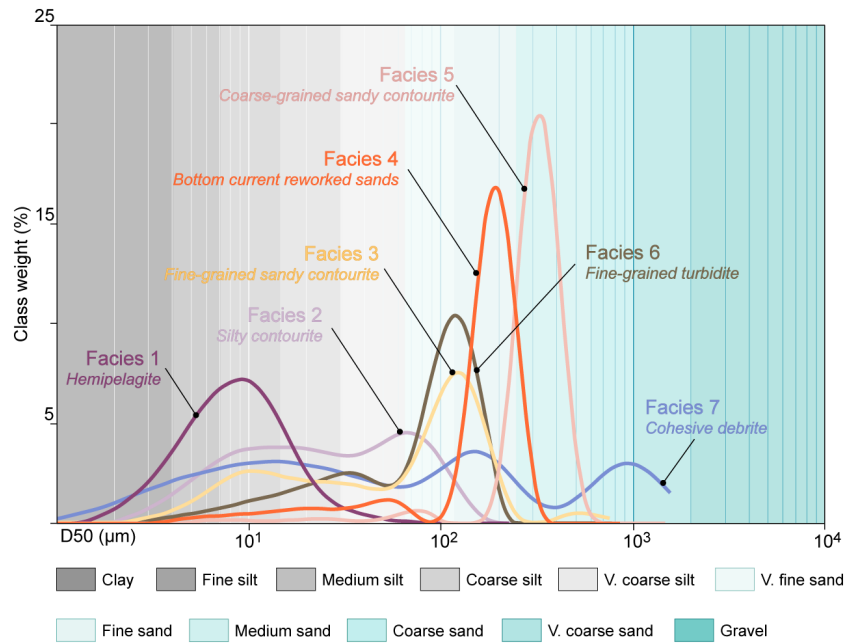


Fig. 6. Grain-size density curves for F1 to F7. The grain-size distribution curve can vary slightly for each facies, and the most representative curves were selected

Facies 1 (F1): homogeneous fine-grained silt

Facies 1 is characterized by massive fine-grained to medium-grained silt (3.6 to 13.9 μm) with sharp or gradational bottom and top contacts (Figs 3 and 4A). Facies thickness is highly variable but never exceeding 17 m. This facies is characterized by the presence of scarce discrete trace fossils, mainly *Planolites*, infilled by silt similar to the host material, making it difficult to distinguish traces (Fig. 4A). The sediment is poorly to very poorly sorted (Fig. 5A and B). The grain-size distribution is predominantly unimodal, mesokurtic, with symmetrical skew at Site U1388 and coarse to symmetrical skew at Site U1389 (Figs 5C and 6). The cumulative frequency curve shows a smooth S-shaped curve with a narrow base and top (Fig. 7A).

Based on the thin section analysis, F1 shows a massive, matrix-supported texture with quartz and feldspar grains ranging from coarse-grained silt to (scarce) very fine-grained sand (Table S1). Whilst the matrix consists of brownish detrital clays, it also has a variety of other components (Fig. 8A). They include silt-grade quartz and feldspar grains, and opaques including authigenic pyrite. Carbonates occur in the form of both fine-grained bioclastic material and microcrystalline authigenic material. Apart from occasional planktonic foraminifera, bioclasts constitute abundant small, often recrystallized, fragments (Fig. 8A).

Facies 2 (F2): alternated fine-grained to coarse-grained silt

Facies 2 consists of mottled fine-grained to coarse-grained silt (4.7 μm and 67.3 μm). Bed boundaries are usually indistinct (Fig. 3). This facies is comprised of 4 to 10 m thick intervals. Fine-grained silt intervals are characterized by scarce fine-grained filled traces (*Planolites* and *Scolicia*), and locally with coarse infill (*Planolites* and *Thalassinoides*) (Fig. 3B). Some intervals of F2 consist of well-developed bedsets (up to 5 m thick; Fig. 9) with four to six beds, individually 3 to 60 cm thick. These bedsets show a coarsening–fining upward trend of medium-grained to coarse-grained silt. Each bed may exhibit: (i) a sharp base and gradational top, (ii) a sharp base and top; or (iii) a gradational base and top. Each individual bed is fully bioturbated with abundant *Planolites* and *Thalassinoides* filled by coarser sediment (Fig. 4B and C). The sediment is very poorly sorted (Fig. 5A and B). The grain-size distribution is bimodal and either mesokurtic or platykurtic, with a predominantly symmetrical skew (Figs 5C and 6). The cumulative frequency curve is smoothly S-shaped with a narrow base and top (Fig. 7B).

Microfacies show a matrix-supported texture (Table S1) with coarse-grained silt, although there are irregular pods of more argillaceous material (Fig. 8B). F2 can present thin irregular lamination composed of dark brown to black pyritized material that is also enriched in silt (Fig. 8B). At Site

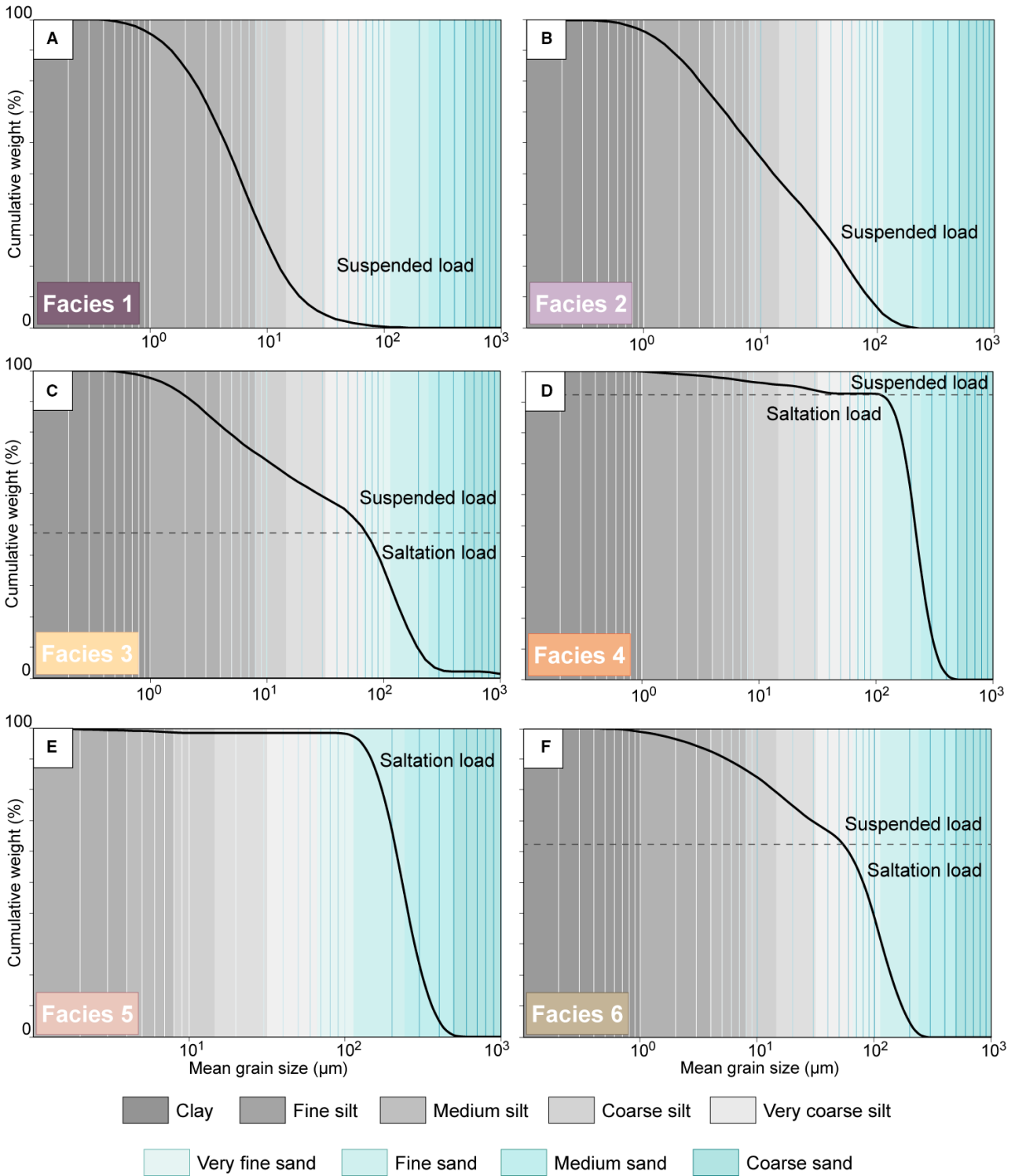


Fig. 7. Cumulative frequency curves for F1 to F6. The curves show an important change in the dominant transport process (suspended and saltation load) between hemipelagic (F1) and coarse-grained sandy contourites (F5), represented by a change in the trend of the curve as proposed by Brackenridge *et al.* (2018). The cumulative frequency axis is in reverse order.

U1388, F2 includes 0.25 to 0.5 mm argillaceous pellets similar to the matrix but devoid of sand grains and with distinctive concentric dark bands rich in organic matter (Fig. 8C).

Facies 3 (F3): mottled coarse-grained silts and fine-grained sands

Facies 3 consists of mottled, medium-grained silt to fine-grained sand (12.4 to 157.0 μm) (Fig. 3). Beds may be: (i) normally and inversely graded; (ii) normally graded with a sharp base; (iii) inversely graded with a sharp top; or (iv) massive with both a sharp base and top. The thickness of F3 varies between 3 cm and 2 m thick. This facies is intensely bioturbated, with coarse-grained filled traces (*Planolites*) distributed in horizons (Fig. 4D to F). The sediment is very poorly sorted (Fig. 5A and B) and has a bimodal grain-size distribution that ranges from platykurtic to very leptokurtic, with a fine to very fine skew (Figs 5C and 6). The cumulative frequency curve shows two parts with different gradients. The upper part presents a concave-up shape and the lower one an S-shape (Fig. 7C).

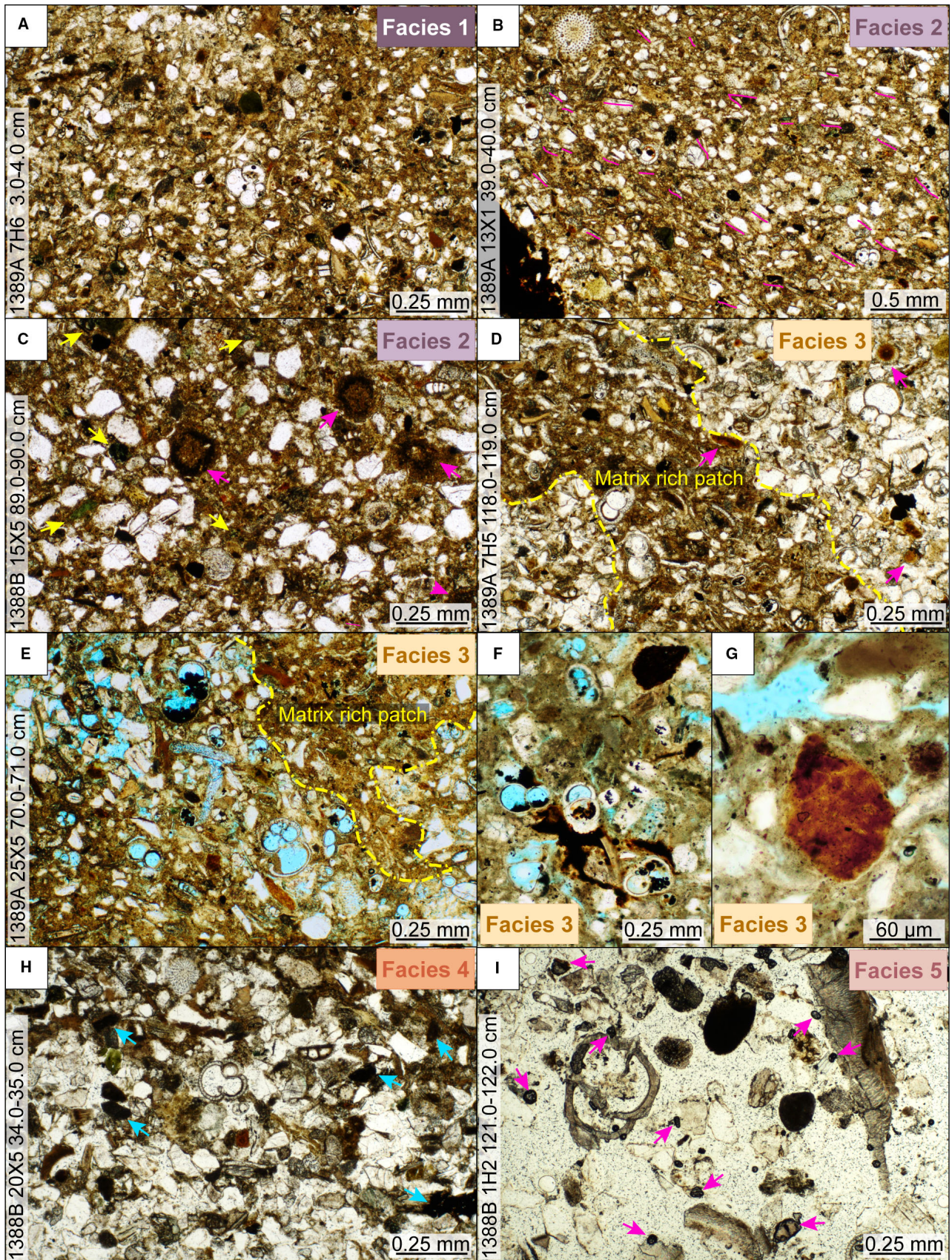
Thin section analysis shows that the matrix content is lower than in other facies (Table S1). Irregular patches that are matrix-rich and matrix-poor are common (Figs 3, 8D and 8E). Some samples include an irregular, sub-horizontal, wavy band up to 2 mm thick, composed mainly of the argillaceous matrix with just a small proportion of coarser particles (Fig. 8D). Subcircular and elongate particles are mostly fragments of foraminifera tests and thin-shelled bivalves. Brown glauconite pellets (Fig. 8G) comprise up to 4.7% of this facies, the highest value among facies.

Facies 4 (F4): cross-laminated sands

Facies 4 consists of rhythmic alternations between coarse-grained silt and lenticular-shaped laminae of medium silt to medium-grained sand (17.9 to 352.2 μm). This facies, between 4 to 10 cm thick, features boundaries with a sharp base and a gradational top (Fig. 4G). Sandy lenses are typically less than 0.5 cm thick but may reach up to 1 cm (Figs 3 and 4G). F4 shows scarce bioturbation, consisting of coarse-grained filled *Planolites* (Fig. 4G). The sediment sorting ranges from poorly sorted in coarse-grained silt intervals to moderately sorted in fine-grained sand intervals (Fig. 5A and B). The grain-size distribution of this facies is bimodal and ranges from platykurtic to very leptokurtic with a predominantly very fine skew (Figs 5C and 6). The cumulative frequency curve shows two parts having contrasting gradients and an accentuated diminution of the base. The upper part has a gentle gradient that abruptly changes to a much steeper lower part (Fig. 7D).

Thin section analysis gives a lower matrix content compared to most of the other facies (Table S1). The rhythmic alternations consist of irregular sub-horizontal banding, 1 to 5 mm thick, associated with varying sand to matrix proportions (Fig. 3). The two interlaminar elements include very fine grain-supported sand and mud-supported sand (Fig. 8D). The grain-supported laminae consist of subrounded to angular and moderately to well-sorted monocrySTALLINE quartz grains (Fig. 8H). The matrix-supported laminae also consist primarily of subrounded to angular but only moderately sorted monocrySTALLINE quartz grains. Bioclast fragments are relatively abundant, mostly in the form of sand-sized unclassified fragments, many

Fig. 8. (A) Matrix-supported F1 texture. F1 is rich in detrital particles. No significant lamination is present but occasionally consists of several small irregular patches of matrix-rich material. (B) Matrix-supported F2 texture with thin irregular bands that are slightly richer in elongated particles which mark poorly defined sub-horizontal lamination (pink lines). A few fragments and thin irregular laminae of dark-brown to black pyritized material occur, as seen in the lower left of this image. (C) Matrix-supported F2 texture. Note the presence of pellets of argillaceous material with concentric organic matter bands (pink arrows). Small green glauconite pellets are moderately abundant within this facies (yellow arrows). (D) and (E) Irregular patches of matrix-rich and matrix-poor material that characterize F3, probably representing an originally more regular sedimentary lamination that was disturbed by bioturbation. Foraminifera infilled with brown glauconite and pyrite are common (pink arrows). (F) Small foraminifera infilled by frambooidal pyrite, and (G) the abundant brown glauconite grains present in F3. (H) Grain-supported F4 texture with abundant opaque minerals (blue arrows) that mainly consist of pyrite, especially within foraminifera, along with pyritized fragments. (I) Image of F5 showing the occurrence of completely disaggregated medium-grained sand. Most of the field-of-view is comprised mounting resin, which accounts for the very high modal-analysis porosity. Lithic fragments are relatively abundant (3.95%), and mainly consist of mica schist. Zircons are abundant in this facies (pink arrow). Microfacies images were taken with plane polarized light (PPL).



of which are recrystallized. The modal analysis indicates that opaques are more abundant here (1.8%) than in other facies (Table S1; Fig. 8F).

Facies 5 (F5): massive medium-grained sands

Facies 5 consists of massive fine-grained to coarse-grained sands (181.8 to 544.5 μm), occasionally interbedded with beds consisting predominantly of shell fragments (Figs 4H and 6H). Discrete trace fossils are difficult to differentiate in this relatively coarse-grained facies. The sediment is predominantly well-sorted but occasionally poorly sorted in the shell-rich beds (Fig. 5A and B). The interbedded beds with shell fragments display inverse grading from fine-grained to medium-grained sand, and then normal grading from medium-grained to fine-grained sand (Fig. 4H). The grain-size distribution of this facies is unimodal and ranges from mesokurtic to very leptokurtic with a predominantly very fine skew (Figs 5C and 6). The cumulative frequency curve shows two different gradients: the upper part is almost horizontal, whereas the lower part is sharp (Fig. 7E). F5 is distinguished only in Site U1388 (between 0 mcd and 3.5 mcd).

Thin sections from F5 show unconsolidated clean sand (Fig. 3). Quartz and feldspar grains are mostly of fine-grained to medium-grained sand size. Bioclasts make up a large proportion of this facies (Table S1) and consist of relatively large (several millimetres) fragments of bivalves, foraminifera, echinoids and occasional smaller fragments of probable calcareous algae (Fig. 8I). Zircons are abundant in this facies (Fig. 8I).

Facies 6 (F6): normally graded thin-bedded sands

Facies 6 consists of fine-grained silt to fine-grained sand (11.7 to 201.54 μm) beds (Fig. 3). Beds are either: (i) massive with both a sharp base and top (Fig. 4C); or (ii) normally graded with a sharp base (Fig. 4I). The bed thickness of F6 usually amounts to 3 to 4 cm. This facies is scarcely bioturbated with coarse-grained filled *Planolites* and *Thalassinoides* at the top of the beds (Fig. 4I). The sediment is very poorly sorted (Fig. 5A and B) and the grain-size displays a predominantly platykurtic bimodal distribution with a fine to very fine skew (Figs 5C and 6). The cumulative frequency curve shows two different gradient trends, similar to the F3 distribution; yet here the upper part shows a concave-up shape (Fig. 7D).

Facies 7 (F7): bioclastic conglomerate

This facies consists of bioclastic fragments in a coarse-grained silt to very fine-grained sand matrix (34.63 to 109.5 μm). The facies has sharp basal and top contacts (Fig. 4J). The thickness of F7 ranges from 10 to 35 cm (Fig. 4J). No trace fossils were observed. The sediment is structureless and predominately composed of both fragmented and complete shells, generally between 0.5 mm and 3.0 cm in size (Fig. 4J). The matrix sediment is very poorly sorted (Fig. 5A and B), with a polymodal grain-size distribution that is predominantly platykurtic with a fine to very fine skew (Figs 5C to 6). F7 is only present in Site U1388 (54.43 to 55.57 mcd).

Facies Associations

Some of the seven identified facies form vertically related facies associations (FA-A, FA-B, FA-C and FA-D). These associations are described below.

Facies Association A (FA-A) involves F1 and F2 (Fig. 4C) and comprises the largest recovered proportion of the cores at both sites. Both F1 and F2 are either present as isolated facies (14X in Fig. 9; 8H in Fig. 10) or, more commonly, they are intercalated with each other over significant intervals with thicknesses from 5 to 10 m (13X and 14X in Fig. 9; 8H to 9H, 14X in Fig. 10). This facies association frequently forms inversely-graded and normally-graded rhythmic bedsets (F1–F2–F1) anywhere between 10 cm and 125 cm thick (Fig. 4C). The contact between F1 and F2 is gradual (Fig. 4C). FA-A is rare in Site U1388 ($n = 4$; Fig. 11A) compared to Site U1389 ($n = 22$; Fig. 11B). In this facies association, F1 intervals present scarce fine-grained traces, whereas F2 intervals show fine-infilled (possibly *Planolites* and *Scolicia*) and coarse-infilled (*Planolites* and *Thalassinoides*) traces (Fig. 4C).

Facies Association B (FA-B) consists of ten sequences involving F1, F2 and F3 at Site U1388, and 53 sequences at Site U1389 (Fig. 4D to F). They show either; reverse and normal grading (Fig. 4D), normal grading (Fig. 4E), or reverse grading (Fig. 4F).

1 Inversely-graded and normally-graded sequences have a lower inversely-graded vertically stacked F1–F2–F3 along with an upper normally-graded vertically stacked F3–F2–F1 (Fig. 4D). This association is more abundant and has the most variable thickness in Site U1389 ($n = 27$; Fig. 11B). The sequences are usually

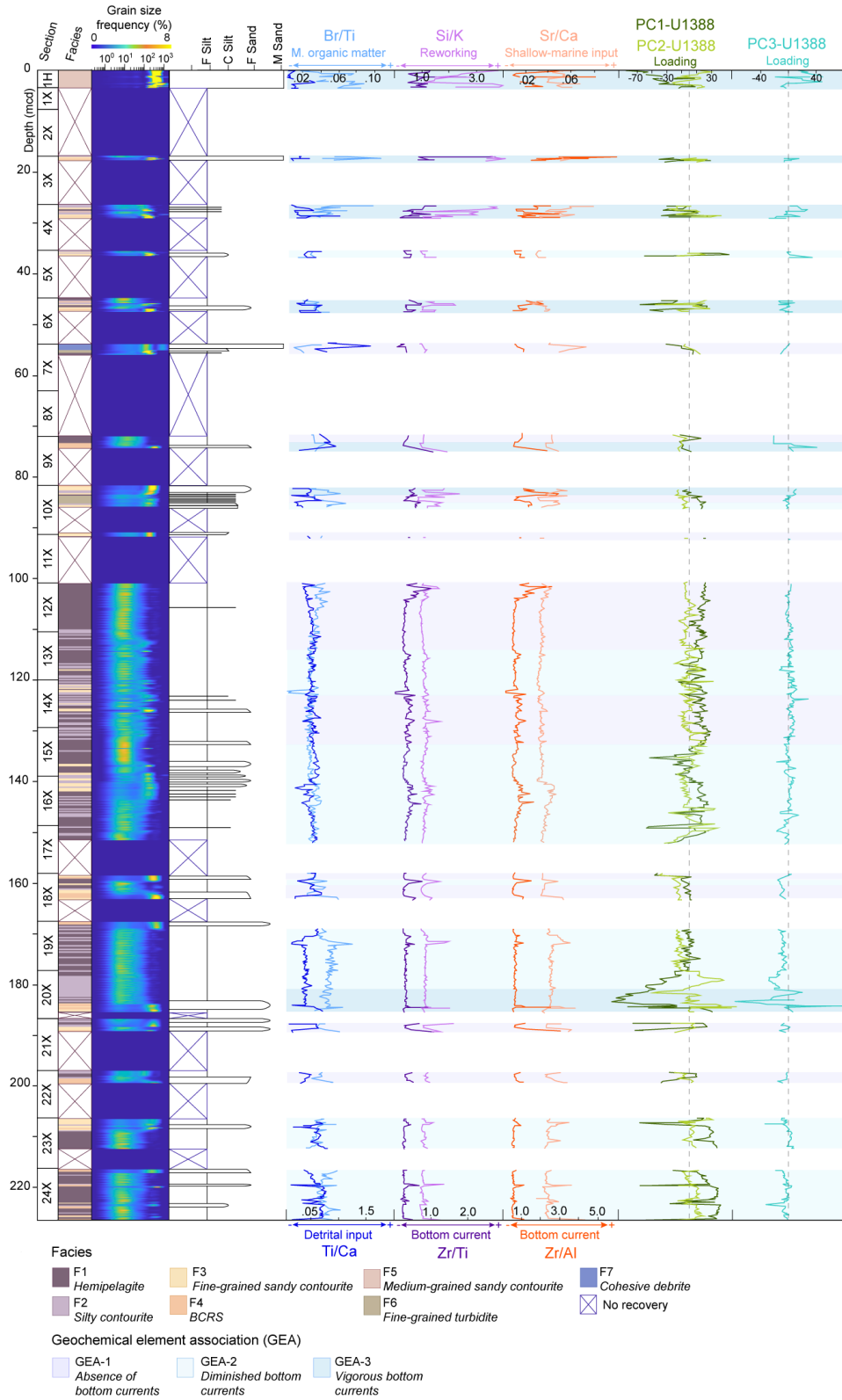


Fig. 9. Grain-size distribution curve and sedimentary facies log plotted against PC distribution and elemental ratios downcore of Site U1388. Coloured bands indicate different geochemical element association intervals. Site U1388 gave poor recovery because of the occurrence of unconsolidated sands (Expedition 339 Scientists, 2012), missing intervals encased in hemipelagites and silty contourites.

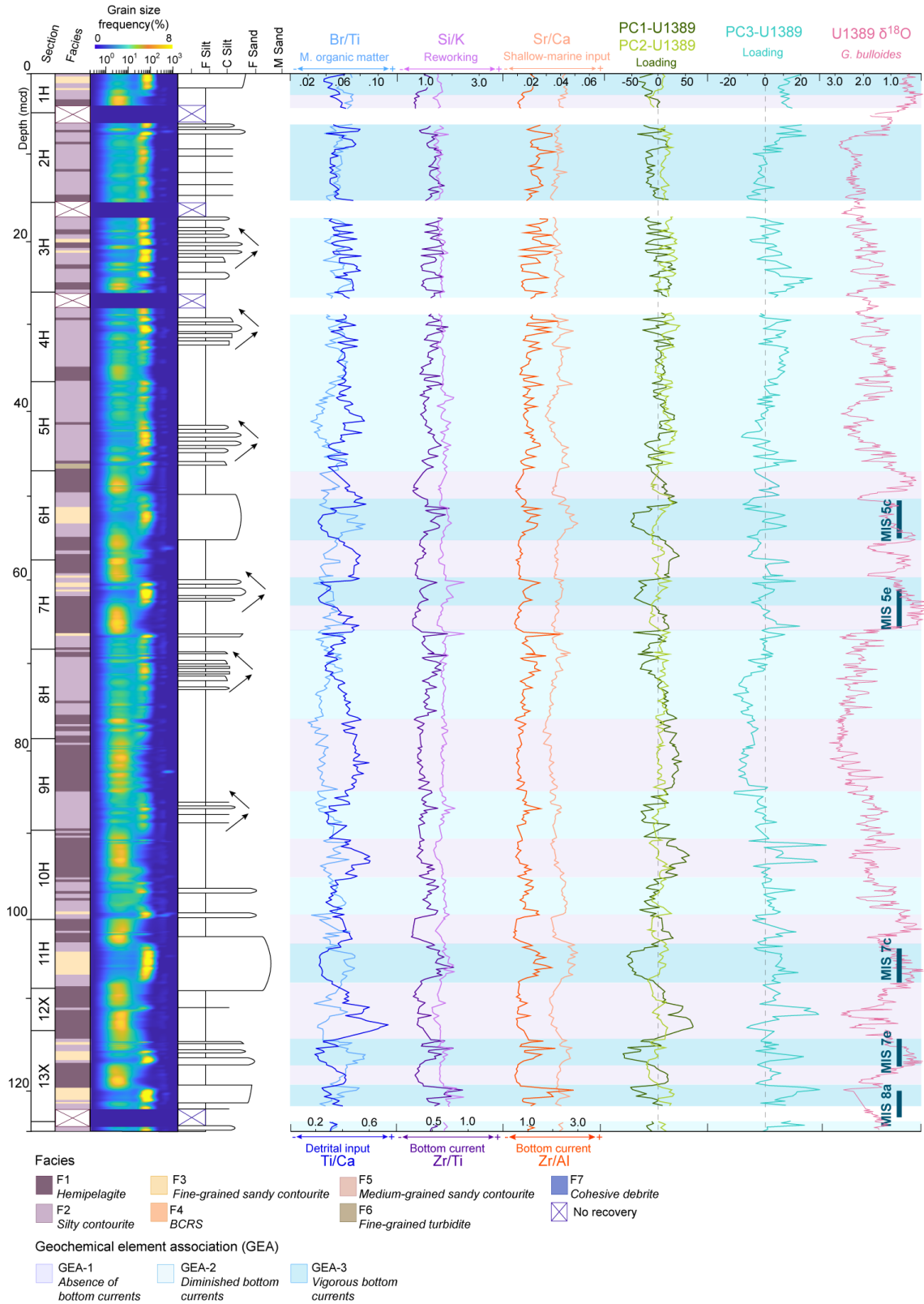


Fig. 10. Grain-size distribution curve, and sedimentary facies log-plotted against PC distribution and elemental ratios downcore of Site U1389 between 0 m and 395 mcd. Coloured bands indicate different geochemical element association (GEA) intervals.

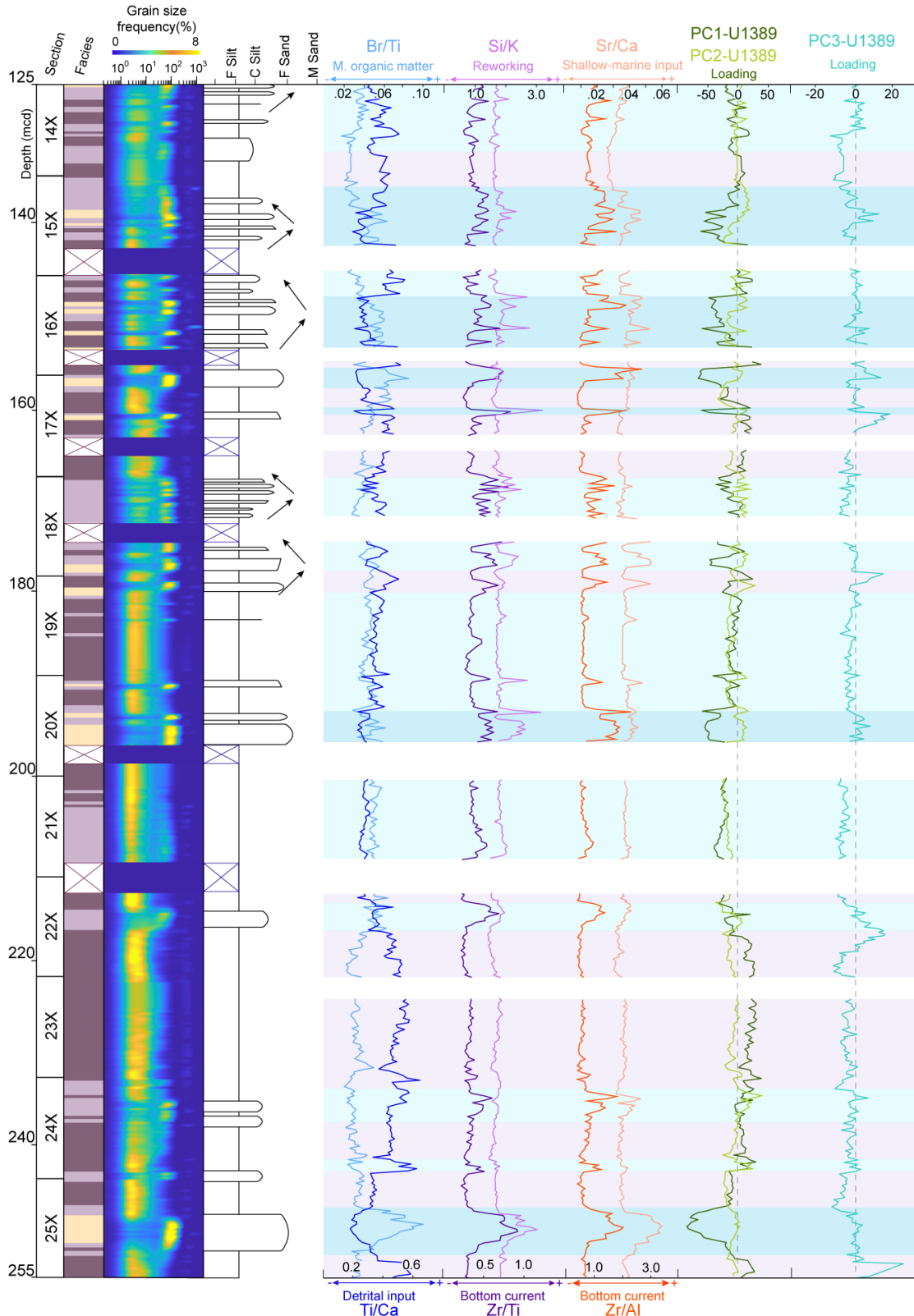


Fig. 10. (continued).

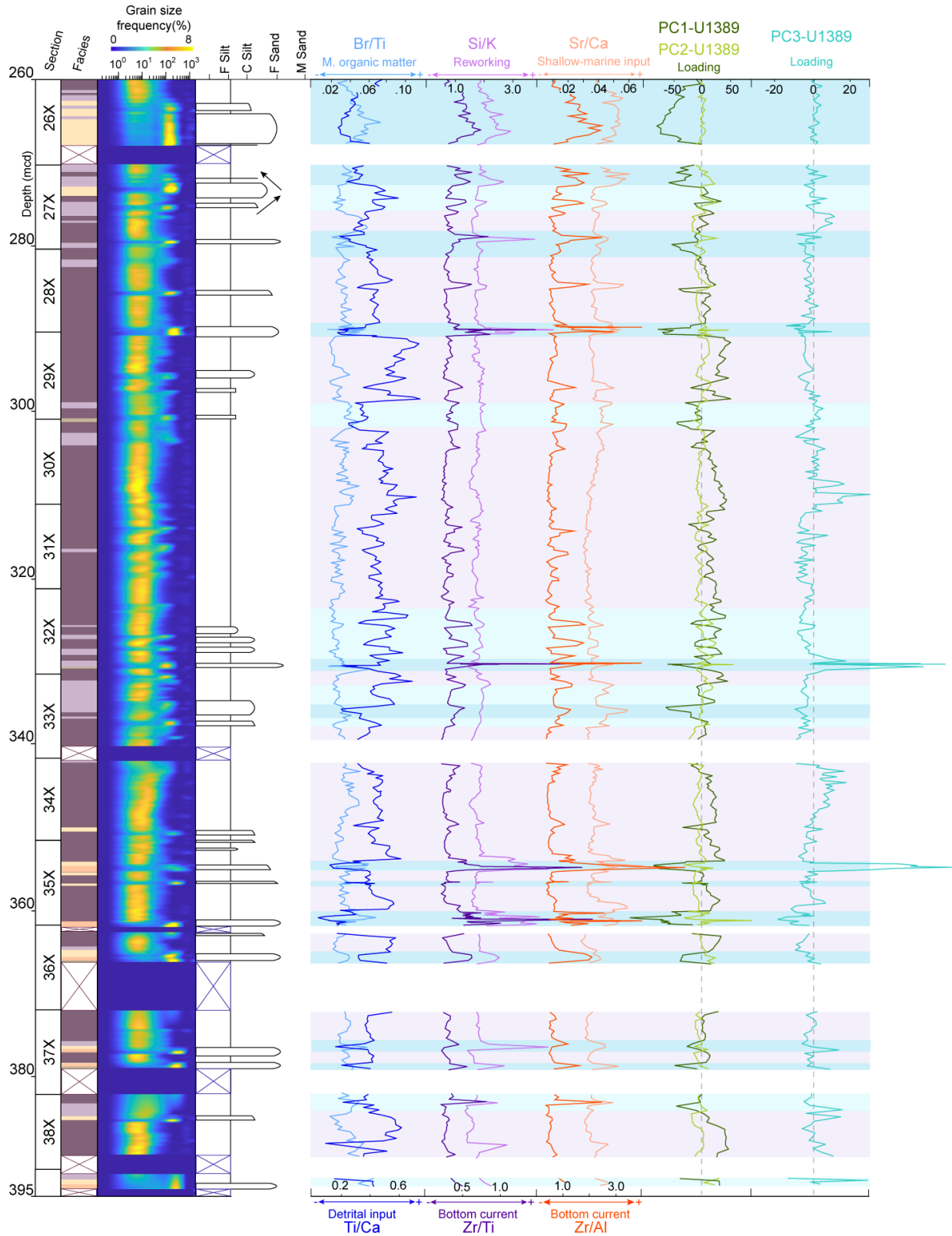


Fig. 10. (continued).

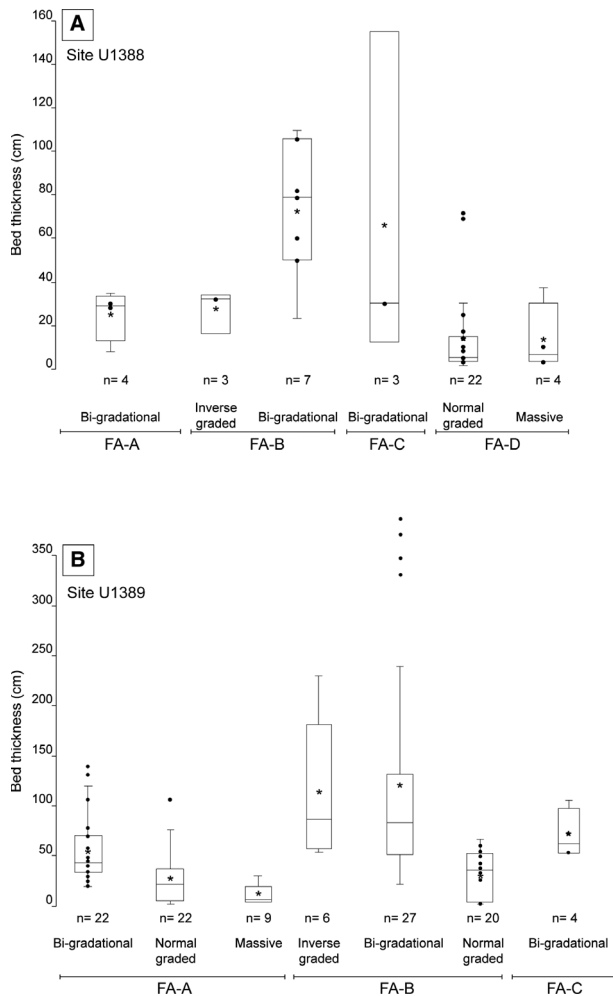


Fig. 11. Thickness and grading characteristics of sandy beds. Box-plots show the direct correlation between average, maximum and minimum thickness of the facies association beds, and the type of grading at Site U1388 (A) and Site U1389 (B).

between 25 cm and 100 cm thick, but they can reach 350 cm in Site U1389 (11H, 25X and 26X in Fig. 10). They are less common in Site U1388 ($n = 9$; Fig. 11A), where they range from 30 cm up to 160 cm in thickness. In this facies association, F1 is characterized by scarce fine-grained filled traces, and the lower F2 shows coarse-grained filled traces (Fig. 4D), whereas the upper F2 is characterized by both fine-grained and coarse-grained filled traces; and, finally, F3 presents abundant coarse-grained infilled *Planolites* and *Thalassinoides*, in some cases distributed in fine horizons (Fig. 4D).

2 Normally-graded sequences consist of the vertical stacking of F3–F2–F1 (Fig. 4E). The contact between F1 and F3 is sharp at the base but

more gradual between the transition from F3 to F2 and F1. This association only occurs in Site U1389, where it is the second most common facies association ($n = 20$; Fig. 11B). The thickness of these sequences varies considerably, between 3 cm and 67 cm (Fig. 4E).

3 Inversely graded sequences present a gradual shift from F2 to F3 and a sharp top contact with F1 (Fig. 4F). They are thicker and comprise more variability in thickness at Site U1389 (from 30 to 225 cm thick; Fig. 11B) as opposed to Site U1388 (from 15 to 35 cm thick; Fig. 11A), where they comprise the less common facies association ($n = 3$; Fig. 11A).

Facies Association C (FA-C) consists of a lower inversely-graded vertically stacked F6–F4 and an upper normally-graded and vertically stacked F4–F3–F2–F1 (Fig. 4G). The transition from muddy (F1) to sandier deposits (F6) is abrupt in the lower part of the sequence, then more gradual for the transition from sandier to muddy sediments in the upper part (F4 to F1). These sequences are most often between 20 cm and 100 cm thick, but they reach 160 cm at Site U1388 (Fig. 11). In this facies, F1 shows a scarce presence (*Thalassinoides*) or absence of discrete trace fossils, while F2, F3, F4 and F6 present coarse-grained filled burrows (*Planolites* and *Thalassinoides*) that may be isolated or concentrated in one or several horizons (*Planolites*) (Fig. 4G).

Facies Association D (FA-D), present only in Site U1388, consists of vertically stacked F1–F6–F1–F7 (Fig. 4I and J). It shows either: (i) massive F6 or F7 with sharp top and bottom contacts (Fig. 4C) or; (ii) normally-graded F6 with a sharp and erosive base and gradual top contact (Fig. 4I). Massive sequences are rare ($n = 4$) and between 3 cm and 35 cm thick, whilst normally-graded beds are more abundant ($n = 22$; Fig. 11A) and can be as much as 72 cm thick, although usually between 3 cm and 5 cm thick (Fig. 4I). F1 and F7 intervals are not bioturbated; F6 intervals present scarce coarse-grained filled *Planolites* and *Thalassinoides* (Fig. 3I).

Statistical analyses

The PCA gave three significant principal components (PC1, PC2 and PC3) for Site U1388 and for Site U1389 (Table S2). The first three axes of the PCA in Site U1388 yield respective variance percentages of 46.9%, 12.8% and 10.0%, accounting for 69.7% of the total variability (Table S2).

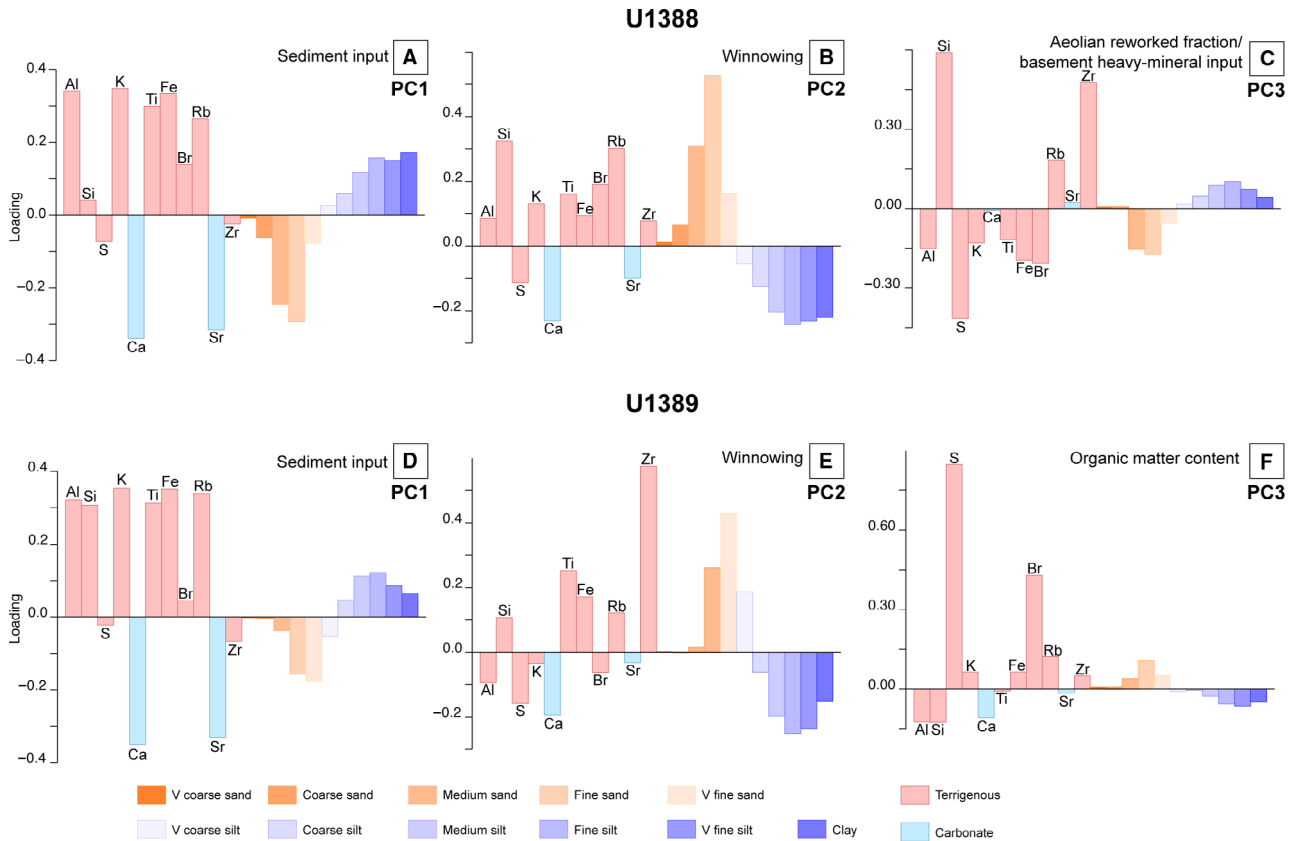


Fig. 12. Principal Components (PC) of Site U1388B (0 to 225 mcd) (A) to (C) and of Site U1389A (0 to 390 mcd – metres composite depth). (D) to (F). VC, Very coarse; C, Coarse; M, Medium; F, Fine; VF, Very fine.

At Site U1389, the first three axes of the PCA represent variance percentages of 55.7%, 11.3% and 8.1%, which amount to 75.1% of the total (Table S2).

The main positively loaded PC1 at Site U1388 are Al, K, Ti, Fe and Rb in the silt–clay fraction against the main negatively loaded Ca and Sr in the sand fraction (Fig. 12A). The main positively loaded PC1 at Site U1389 are Al, Si, K, Ti, Fe and Rb in the silt and clay fractions, as opposed to the main negative Ca and Sr in the sand fraction (Fig. 12D). The cross-plot of sorting against PC1 is very significant for discriminating the sedimentary facies (Fig. 13).

The main positively loaded PC2 at Site U1388 are Si and Rb in the sand fraction against the main negatively loaded S, Ca and Sr in the silt–clay fractions (Fig. 12B). In U1389, PC2 shows a dominant positive loading of Zr and Ti in the sand fraction as opposed to the negatively loaded Ca and S in the silt and clay fractions (Fig. 12E).

At Site U1388, the main positive loadings for PC3 are Si and Zr in the silt–clay fractions

against S, Fe and Br in the sand fraction (Fig. 12C). The main positive loadings for PC3 in Site U1389 are S and Br slightly associated with the sand fraction, as opposed to negative Al, Si and Ca in the silt–clay fractions (Fig. 12F).

Geochemical element associations

The three PCs were plotted against the seven differentiated facies, element ratios and grain-size distribution (Figs 9 and 10). In view of the relationships between the PCs and element proxies, three geochemical element associations (GEA-1, GEA-2 and GEA-3) can be discerned (Fig. 14).

GEA-1 consists of high positively loaded PC1 intervals co-occurring with either positively loaded PC2-U1388 or negatively loaded PC2-U1389 (Figs 9 and 10). This element association usually presents high Ti/Ca values and low Br/Ti, Zr/Ti, Zr/Al, Si/K and Sr/Ca ratios, which present the lowest values downcore (Figs 9 and 10). The intervals with this element association are not relatable to any previously defined facies association. However, when

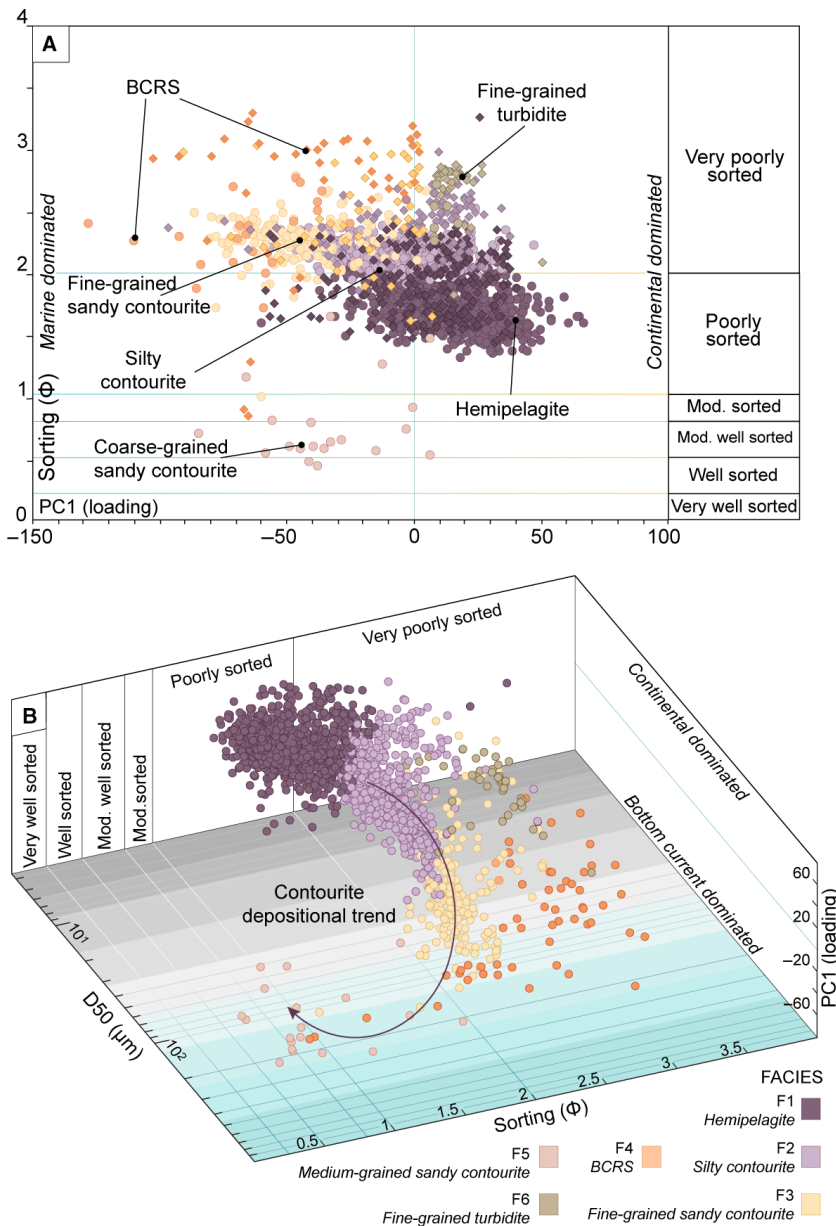


Fig. 13. (A) Cross-plot of sorting (Φ) against PC1 shows that the vast majority of the dataset is located between the very poorly and poorly sorted fields, centred around zero values of PC1. Site U1388 samples of F1, F2 and F6 give positive values for PC1 (between 0 and 45). The samples are even more poorly sorted. F4 (very poorly sorted) and F5 (well-sorted) show a negative loading for PC1. At Site U1389, F1 shows the highest positive values of PC1, whilst F2 drifts to less sorted and to negative values of PC1. F3, F4 and F5 trend towards negative loadings in PC1 and better sorting. Note how F5 can present as positive PC1 despite being a contourite, because this trend reflects the shell-rich beds/lenses (see text for further discussion). The difference in colours between U1388 (rhomboids) and U1389 (circles) highlights the distinctive trends between sites. (B) 3D plot of sorting (Φ), PC1 and D50 showing the contourite depositional helical trend towards better sorting and marine-dominated conditions.. BCRS, bottom current reworked sands.

PC2 is negative, it generally consists of F1 and F6 (8X in Fig. 9; 23X and 30X in Fig. 10) and when PC2 is positive, it consists of F2 (20X in Fig. 9; 2H and 18X in Fig. 10).

GEA-2 consists of negatively loaded or zero values for PC1 combined with positively loaded or zero values for PC2-U1389 (coarse sand with heavy minerals) and PC2-U1388 (fine carbonates) and peaks in PC3-1389. This element association shows parallel trends between Zr/Ti, Zr/Al, Sr/Ca and Si/K without important changes in Br/Ti and Ti/Ca (19X in Fig. 9; 14X and 32X in Fig. 10). These intervals are usually recognized in FA-A. Although minimum Zr/Ti values are found in F1,

intervals with F2 laminations are also characterized by slightly elevated Zr/Ti values (Fig. 10).

GEA-3 consists of strong negatively loaded PC1 in combination with positively loaded PC2 and PC3 values. It usually presents high Br/Ti and low Ti/Ca ratios: Sr/Ca, Si/K, Zr/Ti and Zr/Al show the highest values in this geochemical element association (1H and 4X in U1388, Fig. 9; 25X and 35X in U1389, Fig. 10). This association coincides with facies F3, F4 and F5. Br/Ti exhibits some variability within F4 and F5 (between 0.04 and 0.08), with relative higher ratio values in F3 (up to 1.0 Br/Ti ratio) (Fig. 14). F3 and F5 present the lowest values in Ti/Ca (Figs 9 and

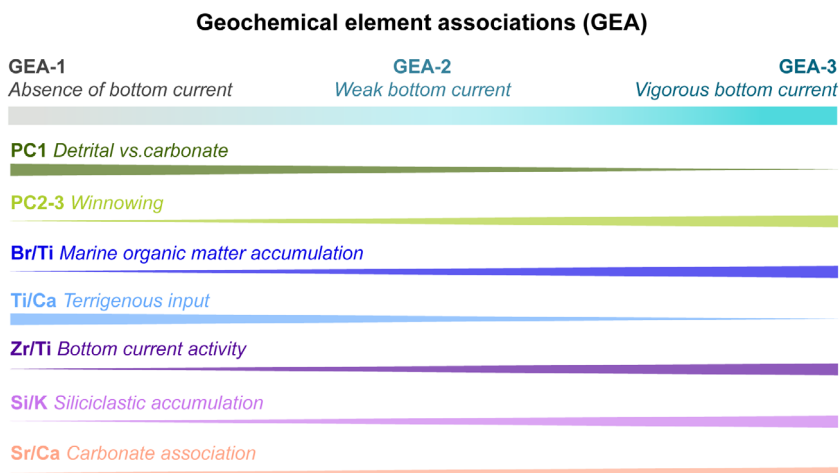


Fig. 14. Sketch of geochemical element associations, with indication of the relationships between different proxies used in this work.

10). The Zr/Ti ratio varies between 0.4 and 1.5, its highest values pertaining to F3.

INTERPRETATION

Principal component analysis interpretation

The positively loaded PC1 corresponds to aluminosilicates in the fine-grained fraction, indicating a terrigenous input (Fig. 12A and D). The negative loaded PC1 (Figs 9, 10 and 15) corresponds to the sandier fraction of the sediment associated with carbonate input (Ca and Sr), suggesting a marine supply. PC1 can therefore be interpreted, at both sites, as a measure of carbonate versus terrigenous sediments as suggested by previous studies based on marine systems (e.g. Bahr *et al.*, 2014; van den Berg *et al.*, 2018).

PC2 shows different loading characteristics for the two sites. The Site U1388 negative loadings for PC2 represent the carbonate fine-grained fraction of the sediment (foraminifera and coccoliths), whilst the positively loaded elements represent the detrital coarser fraction of the sediment (Fig. 12B). Therefore, PC2 signals a different carbonate sediment supply for Site U1388. In turn, the PC2 of Site U1389 is characterized by a high positive loading for Zr with some input of Si in the fine-grained sands (Fig. 12E). During sediment transport, the Zr tends to become more concentrated in fine-grained sand and coarse-grained silt fractions, as does the Ti in finer fractions (Veldkamp & Kroonenberg, 1993; Dypvik & Harris, 2001; Campagne *et al.*, 2016). Therefore, PC2 primarily represents the accumulation of heavy minerals, such as zircon,

in siliciclastic fine-grained sands. Their accumulation would indicate reworking and winnowing under the influence of bottom currents (Giresse & Wiewióra, 2001; Gonthier *et al.*, 2003; Giresse, 2008).

The significance of PC3 is minor (<10%), and at Site U1388 it resembles the PC2 of Site U1389 in terms of the accumulation of heavy minerals (Fig. 12C and E). However, in PC3-U1388 the accumulation of Zr and the enrichment of Si only affect the finest fraction of the sediment. These proxies have been related to enrichment in fine heavy minerals accompanied by fine-grained quartz, owing to aeolian sedimentary input from the Sahara Desert (Moreno *et al.*, 2006; Scheuven *et al.*, 2013; Jiménez-Espejo *et al.*, 2014). At Site U1389, PC3 shows a clear, strong positive loading of Br (Fig. 12F) that is related to the accumulation and/or preservation of marine organic matter (Ziegler *et al.*, 2008; Nieto-Moreno *et al.*, 2011; Bahr *et al.*, 2014).

Sedimentary facies interpretation

Facies 1: hemipelagites. The fine-grained, matrix-supported texture of this facies and the symmetrical skewness values (Brackenridge *et al.*, 2018) suggest hemipelagic sedimentation from deposition by suspension fallout and lateral advection (Hesse, 1975; O'Brien *et al.*, 1980; Martins, 2003). This interpretation is supported by the dominant presence of detrital grains; high peaks in fine-grained detrital input (Ti/Ca) and high PC1 loading further evidence a hemipelagic origin. The occurrence of distinct peaks in detrital input moreover support that these deposits could be traced to river plumes or glacial melt-water diffusion over specific periods (Stow & Smillie, 2020). However, efficient regional

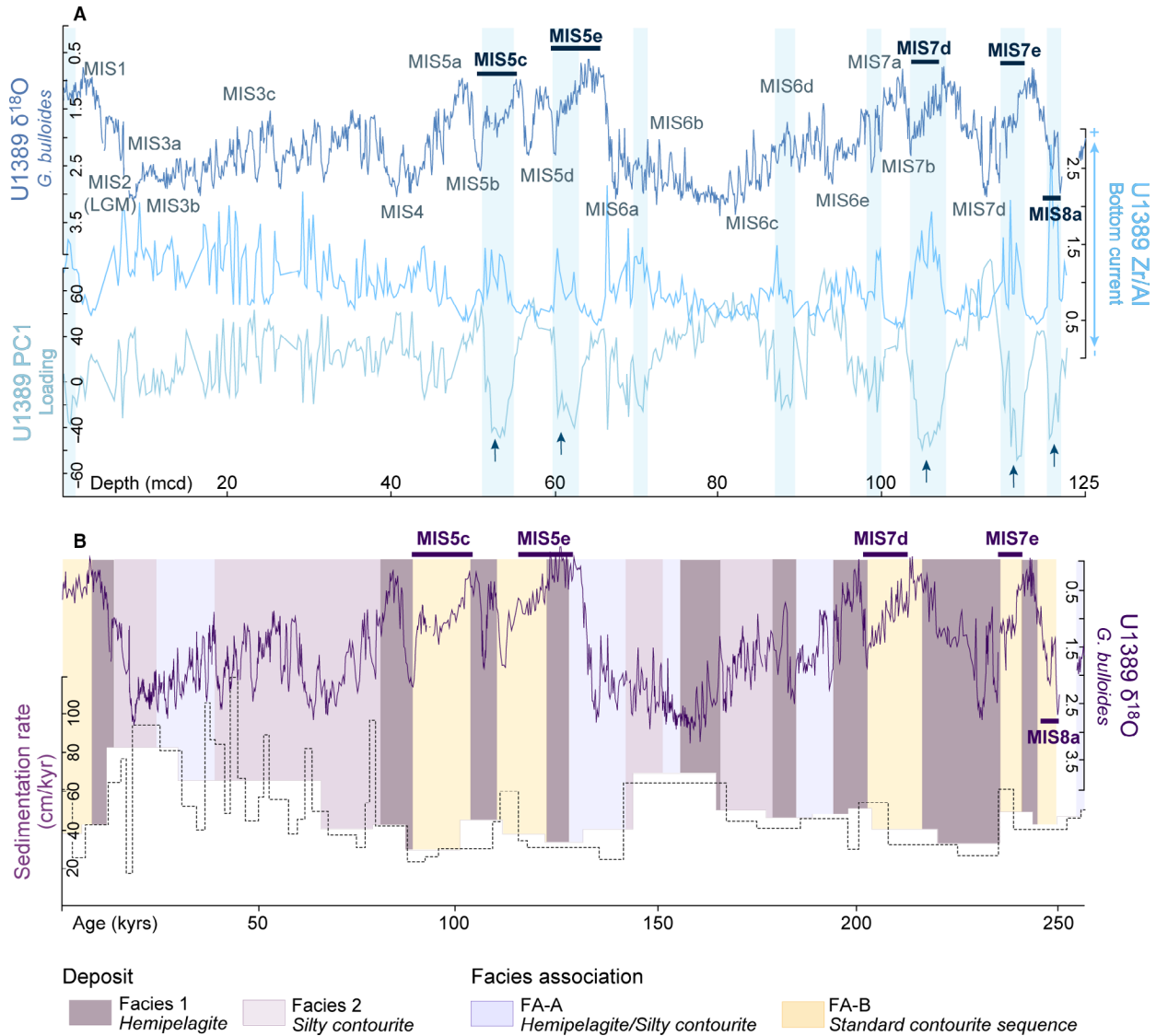


Fig. 15. (A) $\delta^{18}\text{O}$ of *G. bulloides* (dark blue), Zr/Al (light blue) and PC1 (pale blue) from IODP Site U1389 in mcd (metres composite depth) up to ca 250 ka BP. Note a high coherence between the $\delta^{18}\text{O}$ *G. bulloides* curve and glacial–interglacial cycles. PC1 loading displays fine-scale millennial variations that mirror the planktonic $\delta^{18}\text{O}$ curve. A strong correlation exists between the planktonic $\delta^{18}\text{O}$ curve, Zr/Al and PC1 curves during cold stages MIS 5c, 5e, 7d, 7e and 8a. During these periods, PC1 is strongly negatively loaded and Zr/Al curves show their maxima corresponding to cold events during interglacials. The sandier deposits (bold font: MIS 5c, 5e, 7d and 8a) match increases in Zr/Al and high negative loadings in PC1 (black arrows and pale blue bands). There are less important peaks in Zr/Al and negative PC1 loaded intervals that do not present sands. (B) $\delta^{18}\text{O}$ of *G. bulloides* (purple) and sedimentation rates for F1 (hemipelagic), F2 (fine-grained contourites) and FA-A and FA-B from IODP U1389 in age (kyr). Stages MIS 2 and MIS 3 entail fine-grained sedimentation. Stage MIS 6 is characterized by FA-A. The stacking of facies and facies associations shows glacial–interglacial variability with fine-grained sedimentation (F1 and FA-A) during glacial periods, and alternations between F1 and FA-B during interglacial periods. Interglacial sedimentation variability is, however, not uniform throughout all interglacial periods, with FA-B during MIS 5c, 5e, 7d, 7e and 8a. The duration of marine isotope substages (stadials) is based on Railsback *et al.* (2015).

nepheloid transport from slope to basin (McCave & Hall, 2002) should not be discarded.

Ichnological features – such as the scarcity of discrete traces and the difficulty in discerning a

subtle mottled texture in homogeneous sediment – reflect unfavourable conditions for trace-maker identification. Moreover, the lack of evidence of anoxia or oligotrophic conditions points to

relatively high sedimentation rates, which stand as the main parameter impeding intensive bioturbation (i.e. Ekdale *et al.*, 1984; Wetzel & Uchman, 2012).

Hemipelagites represent the lowest energy depositional environment. This interpretation furthermore agrees with the low-negatively loaded PC2-U1389 and PC3-U1388. High PC1 loadings in hemipelagites are a key feature of the GEA-1, linked to the absence of bottom currents (see further discussion below and in Fig. 15). When bottom current reworking or gravity-driven flows are not dominant sedimentary processes, marine productivity and continental input constitute the main mechanism of sedimentation.

Facies 2: silty contourites. Visual discernment between F1 and F2 is difficult at core-scale (Fig. 3B and C). The symmetrical skewness and platykurtic to mesokurtic kurtosis (Fig. 4B), suggests that F2 was deposited through settling from weak bottom currents (0.1 m s^{-1}) with a dominantly fine suspension load (Fig. 7B) (Brackenridge *et al.*, 2018; Yu *et al.*, 2020). The alternating *Planolites* horizons and *Thalassinoides* isolated burrows (Fig. 4B) signals increasing substrate cohesion from softground to firmground conditions, thus indicating that the presence of omission surfaces (Rodríguez-Tovar *et al.*, 2019), is more difficult to see in F1. A lower sedimentation rate with omission surfaces would support continuous, sparsely distributed bioturbation.

In hemipelagites, fine-grained detrital settling is the main sedimentary process within the middle slope. When the intensity of a bottom current is slightly enhanced, quartz-rich detrital grains and heavy minerals start to concentrate, showing an increase in Si and Zr (positively loaded PC2), and the fine-grained detritics are reworked and winnowed. In addition, whilst the hemipelagic deposits are massive, silty contourites show distinctive rhythmical grain-size alternations in most intervals of 3 to 60 cm (5H in Fig. 10). This facies contains well-developed bedsets of coarse-grained silt with sharp or gradual basal and top contacts, suggesting a different depositional process than hemipelagites. The rhythmical variation suggests fluctuations in the bottom current intensities (Stow *et al.*, 2002; Martín-Chivelet *et al.*, 2008; Rebesco *et al.*, 2014; Hüneke *et al.*, 2020), in agreement with the sparsely distributed bioturbation. For these reasons, F2 deposits are interpreted as fine-grained

contourites or, as the silty contourite division of Gonthier *et al.* (1984), corresponding to the C2 and C4 intervals of Stow & Faugères (2008).

Facies 3: fine-grained sandy contourites. Fine-grained sandy contourites are characterized by a general lack of primary sedimentary structures, very poorly sorted sediment and a high level of mixing produced by extensive bioturbation. In contrast to F1 and F2, the inverse relationship between sorting and grain size in this facies occurs approximately at 50 to 60 μm (Fig. 5A), indicating an increase in bedload transport by saltation and the onset of significant winnowing, as suggested by Brackenridge *et al.* (2018) and Yu *et al.* (2020). This is also observed in the cumulative frequency curve: the gradient shift marks a decrease in deposition from suspension, with a greater fraction of sediment coming from the saltation load (Fig. 7C). These are typical depositional trends for sandy contourites, as velocity capacity increases and the finest fraction remains in suspension (Brackenridge *et al.*, 2018). This facies furthermore presents a major concentration of brownish glauconite grains (Table S1; Fig. 8G). The presence of glauconite in contourites is noteworthy as bottom currents usually favour long periods of cation exchange across the seawater/sediment interface, thereby promoting glauconite growth (Giresse, 2008; Tallobre *et al.*, 2019; Hovikoski *et al.*, 2020). The brownish colour of glauconite in this facies (Fig. 8G) could correlate to low sedimentation rates and moderately energetic bottom currents on the seafloor (Tallobre *et al.*, 2019).

Extensive bioturbation resulted in sediment mixing, leading to irregular patches of matrix-rich and matrix-poor sediment (Fig. 5C). Such patches are interpreted as relics of alternating sub-horizontal lamination of well-sorted and less-moderately sorted laminae severely disturbed by bioturbation (de Castro *et al.*, 2020). Several horizons with abundant coarse-filling traces (*Planolites*) suggest that discontinuous sedimentation favoured discrete phases of sedimentary condensation and bioturbation (Rodríguez-Tovar & Hernández-Molina, 2018). As in silty contourites (F2), the alternation of *Planolites/Thalassinoides* as isolated burrows points to increasing substrate cohesion, from softground to firmground conditions, indicating breaks in sedimentation (Rodríguez-Tovar *et al.*, 2019).

The geochemical signal of this facies features a decrease in PC1 and an increase in PC2 coinciding with periods of enhanced bottom current

activity (GEA-3; Figs 9 and 10). When the current speeds up, the fine-grained fraction is winnowed (low Ti/Ca, negatively loaded PC1), and the sediment is enriched in quartz and coarser bioclasts (high Si/K and Sr/Ca, positively loaded PC2), common for sandy contouritic facies (Nelson *et al.*, 1999; Stow *et al.*, 2013a; Capella *et al.*, 2017; Brackenridge *et al.*, 2018). Therefore, the primary PC1 terrigenous input signal is completely overprinted (PC2 in Fig. 12E; PC3 in Fig. 12C). This observation agrees with previous models for contourites, where coarser beds are often degraded by bioturbation and are found in a host sediment once relatively rich in organic matter (Mulder *et al.*, 2013; Stow *et al.*, 2013a). The increase in marine organic matter (Br/Ti) is observed in most of the sandy contourite beds (Fig. 10), where enhanced bottom currents provide higher amounts of nutrients and/or organic matter. It has been proposed that internal waves, facilitate the lateral transport of particulate organic matter, and hence substantially improve the supply of food to sessile organisms (Monteiro *et al.*, 2005; Duineveld *et al.*, 2007; Hebeln *et al.*, 2016; Lim *et al.*, 2018). In addition, peaks in Zr/Ti indicate higher heavy mineral concentrations evoked by stronger bottom currents. Therefore, F3 is the result of bottom current processes pertaining to the sandier central interval of the bi-gradational sequence defined by Gonthier *et al.* (1984), corresponding to the C3 division of Stow & Faugères (2008).

Facies 4: bottom current reworked sands. The locally well-preserved parallel and wavy cross-lamination of F4 are indicative of bedload transport. Lenticular bedding of well-sorted very fine-grained sand lacking matrix is interpreted as ripples. Scarce bioturbation agrees with a high-energy depositional context. This is consistent with predominant deposition from saltation load as interpreted from the cumulative frequency curve (Fig. 7D). This facies usually shows high negative PC1 loading and high positive loading in PC2-U1389 and PC3-U1388, signalling strong winnowing (Fig. 10). Moreover, F4 has strong peaks of Br/Ti, Zr/Al and Zr/Ti, suggesting an increase in marine organic matter and heavy minerals as observed in sandy contourites (F3) (Figs 9 and 10). Bottom currents with higher, but intermittent, velocities would play a role in the deposition of sandy contourites (F3) by enhancing the lateral transport and developing ripples (de Castro *et al.*, 2020). Syndepositional trace fossils (*Planolites*; Fig. 4G) can be

explained by the influence of a sustained bottom current system involving variable strength and sediment concentration (Hovikoski *et al.*, 2020). This facies was previously recognized, studied and interpreted as bottom current reworked sands (BCRS) by de Castro *et al.* (2020).

Facies 5: coarse-grained sandy contourites. The absence of bioturbation in this facies agrees with a fluidized nature of the sand impeding preservation of discrete trace fossils (Expedition 339 Scientists, 2012). Massive and local coarse lag lenses (Fig. 4H) are typical features described for contourite sands deposited in high-energy contourite channels (Brackenridge *et al.*, 2018). The cumulative frequency curve suggests that saltation is the dominant transport process (Fig. 7E): as current velocity and carrying capacity increase, more of the finest fraction remains in suspension and bedload transport becomes more important (Brackenridge *et al.*, 2018). However, the irregular distribution and position of shell fragments in some beds suggests a turbulent process. This facies has moderate sorting; and although it lacks any matrix content, it exhibits varying skewness and kurtosis distributions, which explains the probable action of winnowing at high current speeds (Table S1). The geochemical signature of this facies is characteristic for sandy contourites (F3) and BCRS (F4) with a terrigenous input (PC1) totally overprinted. The strong loading in PC2-U1388 and high Sr/Ca ratios would mark an additional carbonate sediment source – different from Site U1389, where carbonates mainly consist of planktonic foraminifera. In addition, F5 shows high Zr/Al and Sr/Ca ratios, signs of strong bottom current activity and substantial bioclastic input.

These sands were deposited during the Holocene and are sourced from the northern contourite channel of the Gulf of Cadiz, where sandy two-dimensional dunes are identified in a high-energy contouritic channel (Hernández-Molina *et al.*, 2014). Therefore, following the classification of Brackenridge *et al.* (2018), this facies represents coarse-grained sandy contourites resulting from strong winnowing and local erosion at current speeds over 0.5 m s^{-1} (Stow *et al.*, 1998, 2002).

Facies 6: very fine-grained turbidites. Based on erosional features, normal-grading and increasing-upward biogenic structures (Fig. 4C, G and I), F6 is interpreted in the context of waning, dilute, low-density turbidity currents giving

rise to thin-bedded, fine-grained turbidites (Piper, 1978; Stow & Shanmugam, 1980). F6 is poorly sorted, as generally occurs in turbidites (Piper, 1972; Mulder, 2011), due to the concentrated and cohesive nature of mud, trapping silt grains at the head of the turbidity current (Shanmugam, 2002; Mulder, 2011). This is also reflected in the cumulative frequency curve, where the sediment indicates suspended and saltation loads (Fig. 7F). F6 may be visually similar to F3, as some F3 beds share a sharp base and normal grading. However, the geochemical signal is markedly different. Fine-grained sandy contourites are negatively loaded in PC1 and positively loaded in PC2, this being indicative of winnowing (Figs 9, 10 and 13). In contrast, fine-grained turbidites are less sorted and have higher positive loading in PC1 (Fig. 13A and B), indicating a detrital silty/clay terrigenous fraction with a carbonate sandy fraction (PC1 in Fig. 12A). In the cross-plot of sorting versus PC1 (Fig. 13A and B), fine-grained turbidites show a trend opposite to that of fine-grained sandy contourites, with a strong loading of PC1 and less sorting, meaning that the currents did not affect its deposition (Fig. 13). Fine-grained turbidites are additionally characterized by high PC2-U1388 loading, which indicates that they are unusual for the depositional environment, a chief criterion proposed to distinguish fine-grained turbidites (Stow & Piper, 1984). In a setting of turbiditic deposition, isolated coarse-filled discrete traces in F6 (*Planolites* and *Thalassinoides*) could support multiple fine-grained turbiditic events.

Facies 7: cohesive debrites. Facies 7 is interpreted as cohesive debris-flow deposits (Lowe, 1982; Shanmugam, 2012; Pickering & Hiscott, 2015). Mud pockets within the debrite would reflect floating mudstone clasts, indicating freezing of the debris flow in a laminar state (Shanmugam, 2006). The high peak of Sr/Ca and Ti/Ca is related to high contents in shallow-marine bioclasts enriched in aragonite (high Sr) over foraminifera and a terrigenous-rich matrix (Figs 4J and 9). The preservation of shells and lack of fragmentation support a debris flow interpretation, since shells would fragment within turbulent flow. The presence of shallow-marine shells indicates reworking of sediments sourced from the outer shelf/upper slope (Ducassou *et al.*, 2016). An absence of trace fossils evokes unfavourable environmental conditions for trace makers. The fact that these

facies are bound by hemipelagic deposits (F1) suggests they were emplaced during periods without an important influence of bottom currents (GEA-1).

DISCUSSION

Decoding the hydrodynamic energy settings from the geochemical element associations

The PCA score and loading plots are useful in discerning multi-variable elemental changes related to different depositional conditions. The repeated succession of distinctive geochemical element associations (GEA, Figs 9 and 10) can be connected to a sequence of three hydrodynamic energy settings, each characterized by the onset of typical sedimentary processes tied to bottom current activity (Fig. 16).

GEA-1: absence of bottom current

GEA-1 entails fine-grained sediments, indicating low-energy conditions ($<0.1 \text{ m s}^{-1}$; Fig. 16). Under these conditions, when the sediment is composed of fine-grained detrital grains, coarse-grained carbonate is scarce. High loadings in PC1 and peaks in Ti/Ca ratio indicate a dominant supply of terrigenous sediments reflecting low-energy hemipelagic deposition. Low-energy conditions are likewise evident from the low Zr/Ti ratio and negatively loaded PC2-U1389 and PC3-U1388 (Figs 9 and 10), meaning that currents were not able to significantly winnow away the fine-grained particles from the sediment. Within the context of the Gulf of Cadiz, these results indicate that sediments of GEA-1 reflect periods of deposition unaffected by the MOW. During these conditions, hemipelagites, fine-grained turbidites, cohesive debrites and FA-A and FA-D were deposited.

GEA-2: weak bottom current

In GEA-2, PC1 and PC2 values have next to zero loading, with slight divergences in small intervals (13X to 16X in Fig. 9; 4H, 5H, 8H, 21X and 22X in Fig. 10). When the effect of the MOW is gentle, the sediment shows a minimum in PC1 and a minor increase in PC2, indicating a slight enrichment in carbonates (probably foraminifera and coccoliths). In such a trend, the primary PC1 terrigenous input signal is not entirely overprinted by the bottom current activity, instead developing a mixed geochemical signature; and an increase in terrigenous input (Ti/Ca) may be

accompanied by less pronounced Zr/Ti peaks. The Sr/Ca ratio likewise presents peaks, suggesting some enrichment in coarse bioclastic particles. The MOW activity affects the detrital input

and slightly overprints its geochemical signal (0.1 to 0.2 m s^{-1} ; Fig. 16). GEA-2, including predominantly silty contourites, is also related to FA-B.

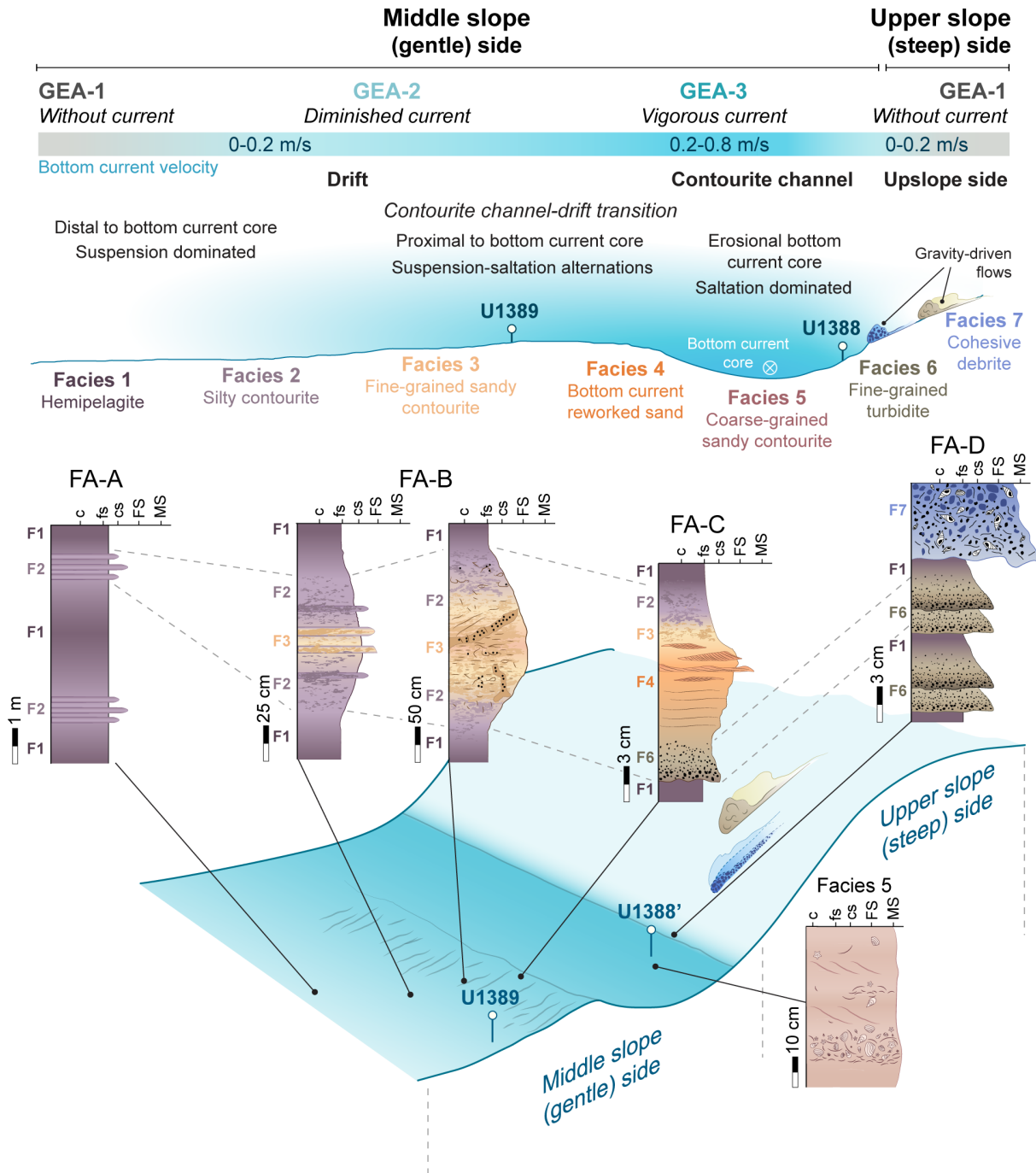


Fig. 16. Conceptual depositional model for the continuous development of facies associations, geochemical element associations and depositional processes in different contouritic physiographic domains. The bottom current velocities in the different contouritic physiographic domains are based on present day measurements (Sánchez-Leal *et al.*, 2017). The location of Site U1388 is a lateral projection, as it is located in a more proximal part of the contourite system.

GEA-3: vigorous bottom current

Corresponding mostly to negative loadings in PC1 (1H in Fig. 9; 11H in Fig. 10), GEA-3 is interpreted as the overprinting of bottom current processes related to PC2-U1389 and PC3-U1388 (Fig. 12C and E). Given these conditions, low values of Ti/Ca compared with GEA-1 and GEA-2 mark a decrease in terrigenous material. When the MOW is enhanced, the coarse-grained carbonate fraction is mainly concentrated (high Sr/Ca) and gives minimum values in PC1. This implies that the coarser carbonates are the most difficult to transport by the MOW on the slope, while the fine-grained detrital material would be more easily winnowed. In addition, these periods witness an increase in Si/K that can be attributed to either a higher siliciclastic input or winnowing of fine-grained particles and concentration of quartz grains.

The fact that PC2 (winnowing) is more strongly expressed at Site U1389 than at U1388 is most likely due to better sorting efficiency at the former (Fig. 5A) and the different nature of material and sedimentary sources reaching the two sites. The positive loading of PC2-U1388 under these conditions (1H, 3X and 20X in Fig. 9) signals the input of a carbonate-rich source, which does not provide sediment at Site U1389. High peaks in the Sr/Ca ratio are seen in this setting (1H in Fig. 9; 11H and 25X in Fig. 10), indicating enrichment in coarse bioclastic particles, as previously observed in sandy contourites in the Gulf of Cadiz (Nelson *et al.*, 1999; Mulder *et al.*, 2013; Stow *et al.*, 2013a). Furthermore, the higher Br/Ti values represent an accumulation or higher preservation of marine organic matter. This is probably tied to lower oxygenation and/or higher organic matter input when the MOW is enhanced in this depositional setting (Jung *et al.*, 1997). GEA-3 includes fine-grained sandy contourites, bottom current reworked sands and coarse-grained sandy contourites, and it is also related to FA-B and FA-C (0.3 to 0.8 m s⁻¹; Fig. 16).

Channel-drift physiographic domains

This shows that the integration of sedimentary facies with geochemical proxies can be used not only to differentiate between depositional environments and sub-environments, but also to establish hydrodynamic changes with respect to the distance of the bottom current core (channel position). Four domains were established (Fig. 16).

Contourite drift background sedimentation (FA-A)

FA-A represents background sedimentation within the middle slope, amounting to 72% of the total recovered core in Site U1388, and 86% in Site U1389 (Fig. 1B), with a low sand/mud ratio of 20 to 30%. The gradual rhythmic intercalations between hemipelagic and silty contourites of FA-A resemble fine-grained bi-gradational sequences with divisions C1–C2 or C4–C5 of the standard contourite sequence (Stow & Faugères, 2008). Hemipelagic deposits usually record a continuum of sedimentary settling and deposition from dilute, very low-density turbidity currents in areas with weaker energy conditions and are therefore placed distally with respect to the contourite channel (Fig. 16).

Hemipelagites are commonly intercalated with contourite muds, indicating low-energy depositional environments. In the same area, present day bottom currents resulting from MOW are very weak (zero or up to 0.1 m s⁻¹) along the drift as compared to adjacent contourite channels (Sánchez-Leal *et al.*, 2017). FA-A is generally tied to alternations of periods without bottom current activity (GEA-1 related to F1) and periods of weak bottom currents (GEA-2 related to F2). The alternations of fine-grained contourites with hemipelagites suggest that the same locations are rhythmically influenced by weak bottom currents supplying/transporting only fine-grained material (Stow & Lovell, 1979; Hüneke *et al.*, 2020).

Contourite drift and drift-channel transition (FA-B and FA-C)

FA-B consists of the standard contourite sequences (C1–C5) proposed by Gonthier *et al.* (1984) and Stow & Faugères (2008). The bi-gradational sequences of FA-B are related to a specific physiographic domain in the drift with respect to the core of the bottom current. Changes in sediment supply, bioturbation and energy conditions are registered, with a lack of primary sedimentary structures in the central (C3) sandier interval due to bioturbation.

The distinctive grain-size trend from F1 to F3, depicted in Figs 5 and 13, coincides with the contourite depositional trend defined by Brackenridge *et al.* (2018) and recently studied in detail by Yu *et al.* (2020). However, the presence of relics (Fig. 8D and E) of alternating sub-horizontal lamination – well-sorted and less well-sorted laminae, severely disturbed by

bioturbation – suggests an intermittent and fluctuating bottom current energy regime (Viana *et al.*, 1998; Shanmugam, 2000; Ito, 2002; Capella *et al.*, 2017; Hüneke *et al.*, 2020). Hüneke *et al.* (2020) suggest that fluctuating bottom currents characterize deposition in all contourite divisions, especially for the C3 division. It is proposed that this intermittency is tied to fluctuations of the main bottom current core energy hydrodynamics, enabling reworking and transport of particles from proximal areas to distal areas with respect to the bottom current core (Fig. 16). Partial sequences with the omission of one or more divisions are also common. In these sequences, normal-graded beds from sandy contourite to hemipelagic (Fig. 4E) are interpreted as base-cut-out sequences (C3–C5; Stow & Faugères, 2008) that reflect a gradual onset of deposition after a period of erosion. Inversely-graded beds, from hemipelagic to sandy contourite (Fig. 4F), are interpreted as top-cut-out sequences (C1–C3; Stow & Faugères, 2008) reflecting increased bottom current velocity up to a point where deposition is no longer possible. Such conditions characterize the drift-channel transitional domain associated with vigorous bottom currents (Fig. 16).

Laminations are better expressed in FA-C, whose heterolithic facies is interpreted as BCRS. The transition from the contourite drift to the drift-channel involves higher velocities, resulting in pronounced winnowing and the development of traction structures. Thus, FA-B is interpreted as a lateral shift to FA-C, marking the drift-channel transition domain (Fig. 16). These BCRS are believed to reflect sedimentary condensation, influenced by both gravity flows and bottom currents (de Castro *et al.*, 2020). The more energetic conditions of the drift-channel transitional domain can be attributed to the main core of the bottom current (see Viana & Faugères, 1998), which allows the finest fraction to remain in suspension. In this domain, bedload transport becomes more important and prevents disruption of primary sedimentary structures due to bioturbation (Fig. 4G). The presence of scarce *Planolites* points to low-sediment concentrations in an oxic setting (Hovikoski *et al.*, 2020), in agreement with the influence of more vigorous bottom currents. The preservation of the turbidite remnant at the base of FA-C demonstrates the intermittent influence of down-slope gravity-driven flows to the contouritic drift (de Castro *et al.*, 2020).

Contourite channel (F5)

Coarse-grained sandy contourites (F5) represent contourite channel facies resulting from the action of dominant bedload transport (Fig. 7E) and sediment winnowing at high bottom current speeds (Fig. 16). Bottom current energy is inferred from grain size and increased winnowing, in agreement with GEA-3. Present day bottom currents resulting from branches of the MOW along the modern contourite channels in the studied area can reach 1 m s^{-1} (Sánchez-Leal *et al.*, 2017). The sandy facies along the contourite channels are associated with a suite of sandy bed forms that includes large sandy dunes (Kenyon & Belderson, 1973; Nelson *et al.*, 1993; Hernández-Molina *et al.*, 2006, 2014; Hanquiez *et al.*, 2007; Stow *et al.*, 2013a; Brackenridge *et al.*, 2018; Lozano *et al.*, 2020).

The sandy deposits within the contourite channels are richer in bioclasts than the other studied facies. Enhanced Sr may indicate the presence of high-Sr aragonite, which is common in shallow-water sediments with bivalves, gastropods and corals (Thomson *et al.*, 2004; Rothwell *et al.*, 2006). Hence, the Sr/Ca proxy may reflect a shallow-marine provenance and a more proximal shelf source. The irregular distribution of shell fragments in F5 suggests a turbulent process of sedimentation rather than traction. Accordingly, bioclastic sediment supply to the contourite channel would indicate modern or ancient shallow-marine deposits coming from the adjacent continental shelf or from the littoral outcropping deposits (Rodero *et al.*, 1999; Lobo *et al.*, 2000, 2010), which are characterized by temperate-carbonate-platform sediment (de Castro *et al.*, 2017). The sediment was eroded, then transported by gravity flows (bioclastic debrites as F7), and finally reworked by the MOW along the contourite channels, as proposed previously by Takashimizu *et al.* (2016).

Upslope side (FA-D)

FA-D represents the upslope physiographic domain. This facies association is only present at Site U1388 because it is closer to the upper slope than U1389 and consists of the intercalation of thin-bedded turbidites and cohesive debrites with hemipelagites (Figs 4I, 4J and 16). The high PC1 positive loading of FA-D suggests that sediments were emplaced in a physiographic domain where the bottom current was not able to rework the sediment (GEA-1; Fig. 16). Low-concentration turbidity currents can feed material to bottom current environments at velocities $<0.5 \text{ m s}^{-1}$

(Hüneke *et al.*, 2020; Miramontes *et al.*, 2020; Stow & Smillie, 2020). According to FA-D and these estimated velocities, bottom currents in this upper slope domain must have been very weak or inexistent (GEA-1; Fig. 9) for the hemipelagic, turbiditic and debritic deposits to be preserved.

Drifting towards a multiprocess depositional model

The range of depositional processes described here suggests that the middle slope of the Gulf of Cadiz has been affected by numerous processes and therefore the sedimentary stacking pattern of a contourite drift and contourite channel was not only built up by pure contourite facies. The frequency and amount of sediment input and the relative persistence and strength of bottom currents is determinant for the predominance of one or another deposit (Fuhrmann *et al.*, 2020), including sediment reworking and winnowing.

Although U1388 is located in a contourite channel with high MOW current velocity at present (Sánchez-Leal *et al.*, 2017), it is adjacent to the upper slope, and therefore prone to be directly affected by gravity-driven flows (Figs 1 and 2). Additionally, because the contourite channel funnelled and concentrated part of the gravity-driven flow in passing, it recorded higher quantities of sediment deposited by gravity currents, so that the preservation potential of these deposits is higher. These findings suggest drastic fluctuations in the hydrodynamic behaviour of the MOW over time. Such intermittence in the long-term and short-term behaviour of the MOW has previously been reported for the late Miocene palaeo-MOW (de Weger *et al.*, 2020).

At Site U1389, bi-gradational sequences are the most abundant type-beds, and they present the greatest variance in thickness (Fig. 11B). The presence of a strong bottom current is required to transport the fine-grained sands from the contourite channel to the drift. This mounded drift is found on the downslope side of a contourite channel (Huelva contourite channel, García *et al.*, 2009), where the current velocity is reduced compared to the flow in the contourite channel (Sánchez-Leal *et al.*, 2017). Recently, de Castro *et al.* (2020) proposed that sandy deposits in the drift represent overbank inputs from the adjacent contouritic channel; that is, they would be part of an external supply of low-density turbiditic flows from the slope during periods when the adjacent channel became more active owing to enhanced

MOW. Most of the sandier beds at this site show increased Sr/Ca, following the same trend as grain size or Zr/Al, and thereby supporting that the sediment feeder of sandy contourites is shallow-marine in origin, led into the channel and the adjacent drift by turbiditic flows (de Castro *et al.*, 2020). According to this proposed model, and especially in the drift-channel transition domain, the sandier overbank events can be traced to a single turbidite-bottom current interaction that exhibited lateral thinning and fining trends. The coarser-grained facies that dominate in proximal parts are seen to transition into finer grained facies in the medial and distal areas (away from the bottom current main core; Fig. 16). Once these sediments are deposited by a low-density turbidity current, bottom currents intermittently rework the sediment, generating parallel lamination and ripples while developing well-sorted sands as the BCRS that may or may not include a component of lateral displacement. More distally from the channel, over the drift, weaker energy conditions prevail, favouring bioturbation that distorts the preservation of primary structures. It is proposed that the C3 division of the contourite sequence entails a number of intermittent events with turbidite-bottom current interaction or alternation, wherein bounding surfaces became amalgamated or lost due to the intense bioturbation.

Time of deposition and controlling factors

The age model, sedimentation rates and their link with facies, facies associations and principal components is shown in Fig. 15. The proposed depositional model is clearly controlled by the hydrodynamics of the MOW (Figs 2, 15 and 16). Based on the results of this study, the intervals of vigorous bottom currents show pronounced astronomical cyclicity and occur at times of Northern Hemisphere summer insolation minima, which are more prominent at eccentricity maxima (Fig. 17). During these periods, an intensified MU flows (Voelker *et al.*, 2015; Bahr *et al.*, 2015; Lebreiro *et al.*, 2015; Kaboth *et al.*, 2016; Table S3) favouring the deposition of FA-B. In contrast, periods with weak or no current occur at times of precession minima/insolation maxima, or during glacials (deeper MOW?), favoured the deposition of FA-A (Figs 15B and 17) along the middle slope.

Consequently, the lateral and vertical distribution of facies associations on the drift would be linked to precession-driven changes in

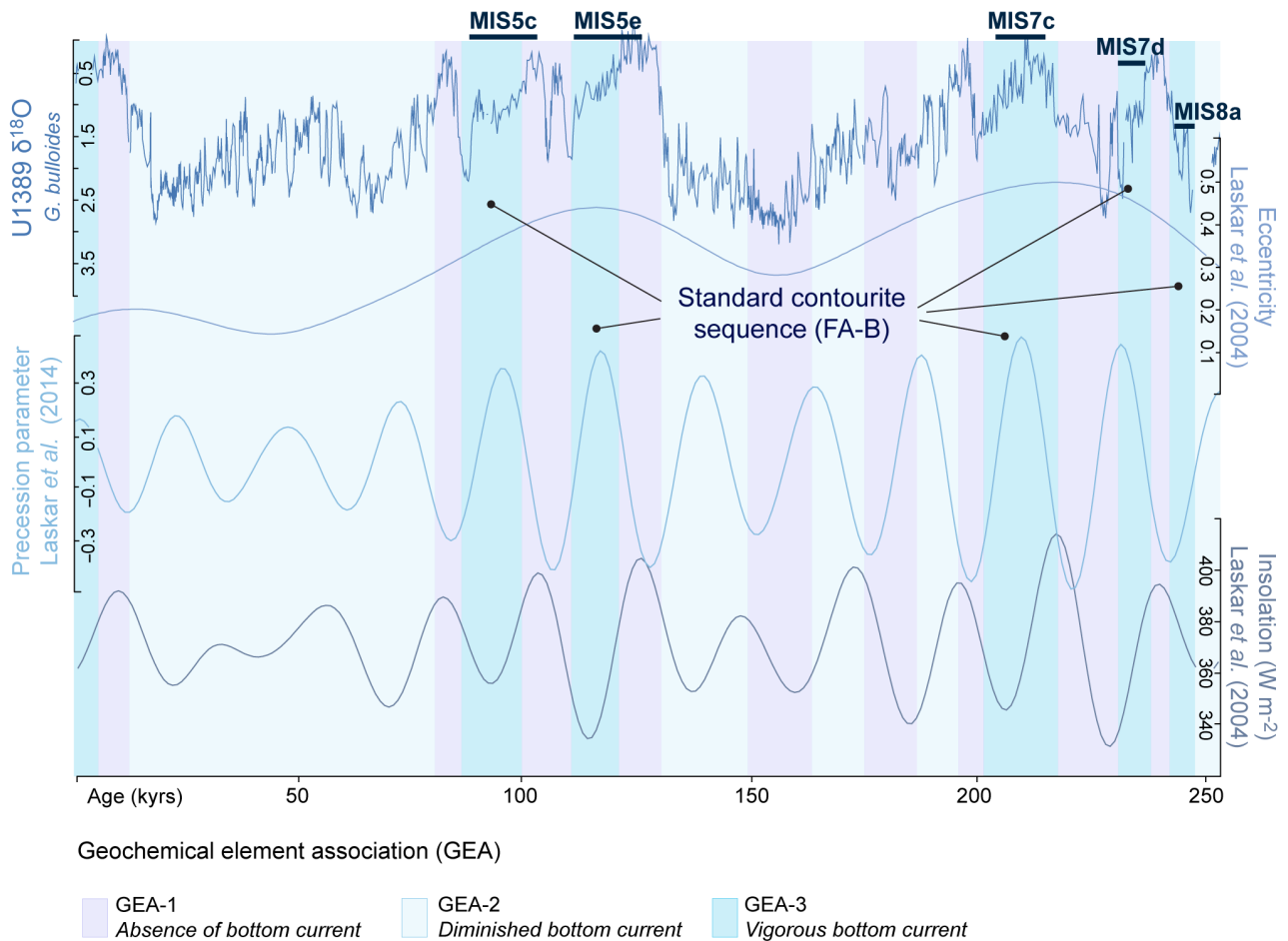


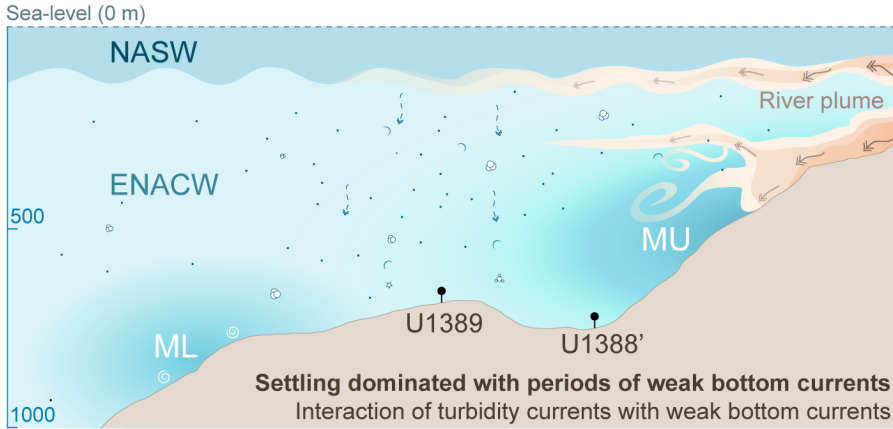
Fig. 17. Comparison of $\delta^{18}\text{O}$ of *G. bulloides* with eccentricity, precession and insolation curves from Laskar *et al.* (2004). Note the overall coincidence of geochemical element association (Mediterranean Outflow Water – MOW – activity) with astronomical cycles.

Mediterranean hydrography punctuated by millennial-scale variability over the past 250 ka (Figs 15 and 17). Dry and cold climate periods during Northern Hemisphere summer insolation minima/precession maxima favoured dense deep-water formation in the Eastern Mediterranean, increasing MOW intensity near the

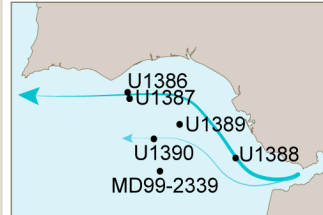
Strait of Gibraltar (Sierro *et al.*, 1999; Toucanne *et al.*, 2007; Bahr *et al.*, 2015; Sierro *et al.*, 2020). Therefore, an intensive and denser MOW is registered during cold substages of Marine Isotope Stage (MIS) 5 (Thomson *et al.*, 1999; Rogerson, 2002; Rogerson *et al.*, 2012; Sierro *et al.*, 2020), MIS 7 (Singh *et al.*, 2015; Sierro

Fig. 18. Conceptual sketch of the scenario in which the Mediterranean Outflow Water (MOW) shoals from cool glacial periods towards the interglacials. The location of Site U1388 is a lateral projection, as it is located in a more proximal part of the contourite system. The projected plan-view location of IODP sites with regard to MOW is based on previous work summarized in Table S3. (A) Interglacial at precession maxima with a slight deepening of the MOW, hence the ENACW–MOW interface would control sedimentary input and favour turbulent sediment transport in the middle slope. (B) Interglacial at precession maxima, where MOW would be slightly shallower. (C) Glacial where the MOW is denser and more saline and flows deeper (modified from Llave *et al.*, 2006; Rogerson *et al.*, 2006, 2012; Lofi *et al.*, 2016; van Dijk *et al.*, 2018). ENACW, Eastern North Atlantic Central Water; IF, Interface; ML, Mediterranean Lower core; MU, Mediterranean Upper core; NASW, Northern Atlantic Surface Water.

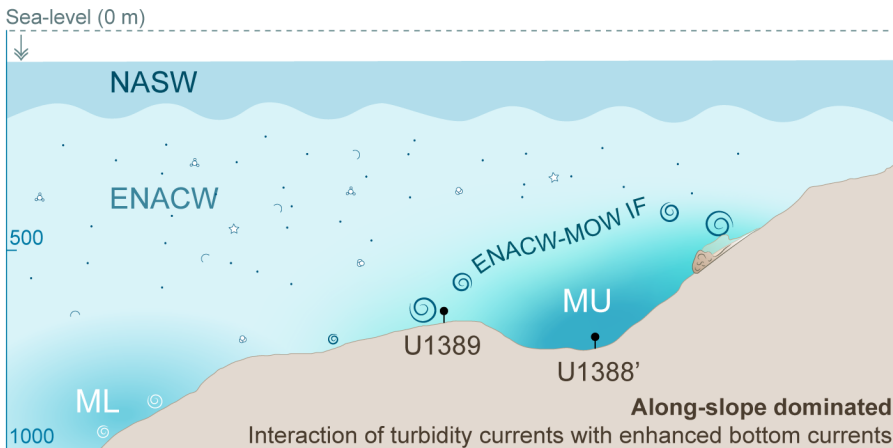
A Interglacial. Precession minima - insolation maxima
Warm and wet stages



Lighter MOW
Shoaling of the MOW
Hemipelagites (F1)
Silty contourites (F2)
FA-A



B Interglacial. Precession maxima - insolation minima
Cold and dry stages



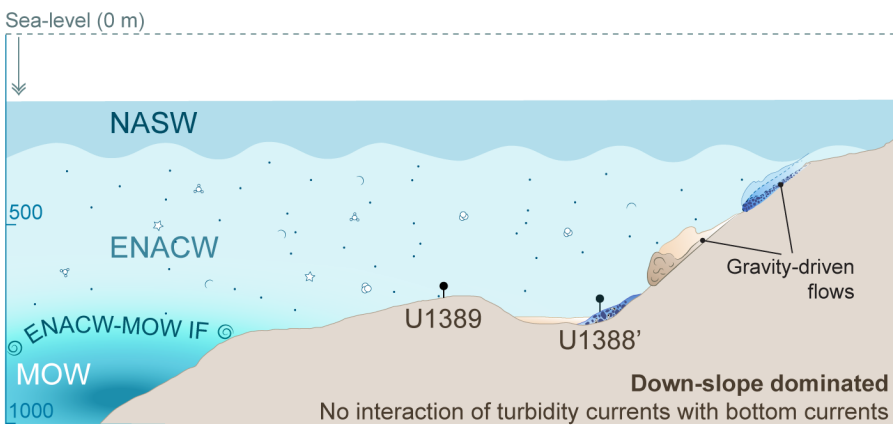
Slight deepening of the MOW
Enhanced lateral particle input

In the drift:
Sandy contourites (F3)
FA-B

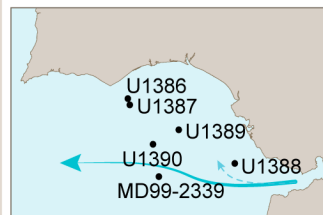
In the channel:
Sandy contourites (F5)



c Glacial



Deepening of the MOW
Hemipelagites (F1)
Turbidites (F6)
Debrites (F7)
FA-A



⊙ ENACW-MOW interface (IF) turbulence

⊙ Settling

et al., 2020), as well as MIS 8, MIS 9, MIS 11 and MIS 12. The intensification of MOW current during these intervals is not only supported by peaks in Zr/Al and high negative PC1-U1389 loadings (Fig. 15A), but also by GEA-3 (Fig. 17). In contrast, at times of insolation maxima/precession minima, the less negative water budget of the Mediterranean associated with higher Nile freshwater discharge reduced dense water formation in the eastern Mediterranean and decreased the intensity of the MOW at Gibraltar, favouring the deposition of FA-A (Fig. 15B) (Bahr *et al.*, 2015; Sierro *et al.*, 2020).

In addition to orbital control, during highstands, typically in interglacial stages (Fig. 18A), the MOW is less dense and located at shallower depths (Schönfeld & Zahn, 2000; Schönfeld *et al.*, 2003; Rogerson *et al.*, 2006, 2012; Llave *et al.*, 2006; van Dijk *et al.*, 2018), circulating over the distal part of the upper slope and the proximal part of the middle slope. This could explain why the most prominent contourite beds occurred during interglacial periods but only at times of precession maxima/insolation minima (Fig. 18B). Llave *et al.* (2006) and Lofi *et al.* (2016) proposed that during these stages, the lower MOW (ML) was regionally weaker than in glacial stages, whilst the upper core of the MU was more vigorous compared to glacial stages. However, during lowstands, a higher sediment supply from gravitational processes (Fig. 18C) is coeval with a denser MOW and a decrease in the vertical density gradient of Atlantic Intermediate Water. As a result, the MOW flows deeper (Schönfeld & Zahn, 2000; Schönfeld *et al.*, 2003; Rogerson *et al.*, 2005; Llave *et al.*, 2006; Voelker *et al.*, 2006; van Dijk *et al.*, 2018; Sierro *et al.*, 2020). Recently, García *et al.* (2020) and Mestdagh *et al.* (2020) proposed that the extension and depth of the ENACW deepened from the upper slope to the middle slope (Fig. 2), as does the MOW–ENACW interface.

Although orbital cyclicity controls sedimentation on the middle slope, changes in facies are also driven by millennial-scale climate variability. During cold and dry stadials (Fig. 18B) the MOW is enhanced, whereas in warm and wet interstadials (Fig. 18A) the MOW decreases (Figs 15A and 17). Sea-level has little influence, although variations in the vertical density gradient of the Atlantic water may bear considerable impact on the settling depth of the MOW (Sierro *et al.*, 2020). Still, minor sea-level oscillations would control sediment input and would favour

sediment transport towards the middle slope by gravity-flow processes (Fig. 18B).

In addition to the millennial scale changes in intensity of the MOW related to Mediterranean climate variability, the vertical and spatial variations of the ENACW–MOW and oceanographic processes associated with its upper interface (internal tides, waves, etc.) are important factors conditioning hydrodynamic energy variations at mid-depths (Vic *et al.*, 2019). Internal waves and pulse-like density fronts arise from instabilities at the interface between highly stratified layers and are hypothesized to play a role in localized drift sedimentation (Preu *et al.*, 2013; Hanebuth *et al.*, 2015; Droghei *et al.*, 2016). Internal waves could move stratified water up and down, creating turbulence able to erode and enhance the lateral transport of sediments and particulate organic matter (Cacchione *et al.*, 2002; Titschack *et al.*, 2009; Pomar *et al.*, 2012; Wienberg & Titschack, 2017; Wienberg *et al.*, 2020). It was recently demonstrated that the ENACW–MOW interface induces internal waves, increasing the delivery of sediments, and favouring the maintenance of coral mound formations at the Porcupine Seabight (Wienberg *et al.*, 2020), or generates sediment waves in the Gulf of Cadiz's upper slope (Mestdagh *et al.*, 2020). Accordingly, associated vertical oscillations of the ENACW–MOW interface would control sedimentary endogenous input and facilitate turbulent sediment transport in the middle slope developing the sandier contourite deposits (Fig. 18B).

CONCLUSIONS

This contribution upholds the use of Principal Component Analysis (PCA) as an essential and quick aid in discriminating hemipelagic deposits from other deep-water sediments affected by bottom current reworking and winnowing processes. The dominant facies and facies associations identified enabled characterization of the background, contourite drift, drift-channel transition, contourite channel and distal upper slope sedimentation. The drift itself is made up of hemipelagites, silty contourites, fine-grained sandy contourites, bottom current reworked sands and fine-grained turbidites. The channel deposits contain coarse-grained sandy contourites, fine-grained turbidites and debrites. They provide evidence that the sedimentary stacking pattern in both the drift and the channel are influenced by a spatial and

vertical interrelation of hemipelagic, gravitational and bottom current processes, seriously questioning the paradigm: drift is merely made up of muddy sediments. Sandy contourite beds are not only common deposits along contourite channels but are likewise present on the drift and in the drift-channel transition.

The time of deposition and controlling factors of the interaction between processes are determined by long-term glacial/interglacial oscillations, although the deposit framework is further defined by high-resolution fluctuations of the Mediterranean Outflow Water (MOW) intensity, sea-level and sedimentary input. Periods with weak or no current occurred at times of precession minima/insolation maxima or during glacials (possibly deeper MOW), favouring the deposition of hemipelagites and silty contourites along the middle slope. The periods of vigorous bottom currents that favour deposition of the standard bi-gradational sequence occur at times of precession maxima/insolation minima. Associated slight vertical shift oscillations of the MOW, hence the East North Atlantic Central Water (ENACW)–MOW interface, would control sediment input and favour turbulent sediment transport in the middle slope of the Gulf of Cadiz. During the interglacial and precession maxima/insolation minima stages, a vigorous upper core of the MOW plus the ENACW–MOW interface had a significant impact on the middle slope through development of sandier contourite deposits.

Further Principal Component Analysis (PCA) and detailed sedimentological, ichnological and geochemical analysis are needed to study contourite depositional systems in both modern and ancient sedimentary records. Drawing comparisons with other continental margins will lead to a better understanding of the importance of bottom current processes and deposits in margin construction overall.

ACKNOWLEDGEMENTS

This project was funded through the Joint Industry Project supported by BP, ENI, ExxonMobil, TOTAL, Wintershall Dea and TGS, within the framework of “The Drifters” Research Group at Royal Holloway University of London (RHUL), in conjunction with the projects CTM 2012-39599-C03, CGL2015-66835-P, CTM2016-75129-C3-1-R, CGL2016-80445-R (AEI/FEDER, UE) and B-RNM-072-UGR18. This research used data and

samples collected by IODP Expedition 339 aboard the Joides Resolution. Data was acquired at the XRF Core Scanner Lab at MARUM – Center for Marine Environmental Sciences, University of Bremen, Germany. Our thanks to Dr Javier Dorador (RHUL, UK) for the high-resolution core imaging treatment, to Dr David Roque (ICMAN-CSIC, Spain) for his help in the hydrographic panels from Fig. 2, and to Dr Angel Puga-Bernabéu (University of Granada, Spain) for revision that helped to improve the original version of the manuscript before submission. This study significantly benefited from discussions with all who attended the IODP Exp. 339 MOW meeting in Heidelberg (Germany) in January 2019. We would like to thank Associate Editor Dr Adam McArthur and the three reviewers, Dr Rachel Brackenridge, Dr Giancarlo Davoli and Dr Adriano Viana, for their positive and constructive comments that helped us improve the manuscript.

CONFLICT OF INTEREST

We declare that we have no commercial or associative aim that might represent a conflict of interest in connection with the work submitted.

DATA AVAILABILITY STATEMENT

The data that support the findings of this study are available from the corresponding author upon reasonable request.

REFERENCES

- Abdi, H. and Williams, L.J. (2010) Principal component analysis. *Wiley Interdiscip. Rev. Comput. Stat.*, **2**, 433–459.
- Bahr, A., Jiménez-Espejo, F.J., Kolasinac, N., Grunert, P., Hernández-Molina, F.J., Röhl, U., Voelker, A.H.L., Escutia, C., Stow, D.A.V., Hodell, D. and Alvarez-Zarikian, C.A. (2014) Deciphering bottom current velocity and paleoclimate signals from contourite deposits in the Gulf of Cádiz during the last 140 kyr: an inorganic geochemical approach. *Geochem. Geophys. Geosyst.*, **15**, 3145–3160.
- Bahr, A., Kaboth, S., Jiménez-Espejo, F.J., Sierro, F.J., Voelker, A.H.L., Lourens, L., Röhl, U., Reichert, G.J., Escutia, C., Hernández-Molina, F.J., Pross, J. and Friedrich, O. (2015) Persistent monsoonal forcing of Mediterranean Outflow Water dynamics during the late Pleistocene. *Geology*, **43**, 951–954.
- Bellanco, M.J. and Sánchez-Leal, R.F. (2016) Spatial distribution and intra-annual variability of water masses on the Eastern Gulf of Cadiz seabed. *Cont. Shelf. Res.*, **128**, 26–35.

- Blott, S.J.** and **Pye, K.** (2001) GRADISTAT: a grain size distribution and statistics package for the analysis of unconsolidated sediments. *Earth Surf. Process. Landforms*, **26**, 237–248.
- Brackenridge, R.E., Stow, D.A.V., Hernández-Molina, F.J., Jones, C., Mena, A., Alejo, I., Ducassou, E., Llave, E., Ercilla, G., Nombela, M.A., Pérez-Arlucea, M. and Frances, G.** (2018) Textural characteristics and facies of sand-rich contourite depositional systems. *Sedimentology*, **65**, 2223–2252.
- Buitrago, J., García, C., Cajebread-Brow, J., Jiménez, A. and Martínez del Olmo, W.** (2001) September. Contouritas: un excelente almacén casi desconocido (Golfo de Cádiz, SO de España). In: *1er Congreso Técnico Exploración y producción REPSOL-YPF*, Madrid, 24–27.
- Bryden, H.L., Candela, J. and Kinder, T.H.** (1994) Exchange through the Strait of Gibraltar. *Prog. Oceanogr.*, **33**, 201–248.
- Cacchione, D.A., Pratson, L.F. and Ogston, A.S.** (2002) The shaping of continental slopes by internal tides. *Science*, **296**, 724–727.
- Campagne, P., Crosta, X., Schmidt, S., Houssais, M.N., Ther, O. and Massé, G.** (2016) Sedimentary response to sea ice and atmospheric variability over the instrumental period off Adélie Land, East Antarctica. *Biogeosciences*, **13**, 4205–4218.
- Capella, W., Hernández-Molina, F.J., Flecker, R., Hilgen, F.J., Hssain, M., Kouwenhoven, van Oorschot, M., Sierro, F.J., Stow, D.A.V., Trabucho-Alexandre, J., Tulbure, M.A., Yousfi, M.Z. and Krijgsman, W.** (2017) Sandy contourite drift in the late Miocene Rifian Corridor (Morocco): reconstruction of depositional environments in a foreland-basin seaway. *Dev. Sedimentol.*, **355**, 31–57.
- Courteney-Jones, W., Quinn, B., Ewins, C., Gary, S.F. and Narayanaswamy, B.E.** (2019) Consistent microplastic ingestion by deep-sea invertebrates over the last four decades (1976–2015), a study from the North East Atlantic. *Environ. Pollut.*, **244**, 503–512.
- de Castro, S., Lobo, F.J. and Puga-Bernabéu, Á.** (2017) Headland-associated banner banks generated during the last deglaciation near the Strait of Gibraltar (Gulf of Cadiz, SW Spain). *Mar. Geol.*, **386**, 56–75.
- de Castro, S., Hernández-Molina, F.J., Rodríguez-Tovar, F.J., Llave, E., Ng, Z.L., Nishida, N. and Mena, A.** (2020) Contourites and bottom current reworked sands: bed facies model and implications. *Mar. Geol.*, **428**, 106267.
- de Weger, W., Hernández-Molina, F.J., Flecker, R., Sierro, F.J., Chiarella, D., Krijgsman, W. and Manar, M.A.** (2020) Late Miocene contourite channel system reveals intermittent overflow behavior. *Geology*, **48**. <https://doi.org/10.1130/G47944.1>
- Dorador, J. and Rodríguez-Tovar, F.J.** (2018) High-resolution image treatment in ichnological core analysis: initial steps, advances and prospects. *Earth Sci. Rev.*, **177**, 226–237.
- Dorador, J., Rodríguez-Tovar, F.J., Expedition, I.O.D.P. and IODP Expedition 339 Scientists** (2014a) Digital image treatment applied to ichnological analysis of marine core sediments. *Facies*, **60**, 39–44.
- Dorador, J., Rodríguez-Tovar, F.J., Expedition, I.O.D.P. and IODP Expedition 339 Scientists** (2014b) Quantitative estimation of bioturbation based on digital image analysis. *Mar. Geol.*, **349**, 55–60.
- Droghei, R., Falcini, F., Casalbore, D., Martorelli, E., Mosetti, R., Sannino, G., Santo-Ieri, R. and Chiocci, F.L.** (2016) The role of internal solitary waves on deep-water sedimentary processes: the case of up-slope migrating sediment waves off the Messina Strait. *Sci. Rep.*, **6**, 36376.
- Ducassou, E., Fournier, L., Sierro, F.J., Alvarez Zarikian, C.A., Lofi, J., Flores, J.A. and Roque, C.** (2016) Origin of the large Pliocene and Pleistocene debris flows on the Algarve margin. *Mar. Geol.*, **377**, 58–76.
- Duineveld, G.C.A., Lavaley, M.S.S., Bergman, M.J.N., De Stigter, H. and Mienis, F.** (2007) Trophic structure of a cold-water coral mound community (Rockall Bank, NE Atlantic) in relation to the near-bottom particle supply and current regime. *Bull. Mar. Sci.*, **81**, 449–467.
- Dypvik, H. and Harris, N.B.** (2001) Geochemical facies analysis of fine-grained siliciclastics using Th/U, Zr/Rb and (Zr+ Rb)/Sr ratios. *Chem. Geol.*, **181**, 131–146.
- Dzulynski, S. and Walton, E.K.** (Eds) (1965) Sedimentary features of Flysch and greywackes. In: *Developments in Sedimentology*. Elsevier Science, Amsterdam, the Netherlands, **7**, 1–274.
- Ekdale, A.A., Bromley, R.G. and Pemberton, S.G.** (1984) Ichnology: the use of trace fossils in sedimentology and stratigraphy. *SEPM Short Course Notes*, **15**, 1–316.
- Expedition 339 Scientists** (2012) Site U1389 Summary. IODP Expedition 339: Mediterranean Outflow. Site Summaries. International Ocean Discovery Program.
- Faugères, J.C., Gonthier, E. and Stow, D.A.V.** (1984) Contourite drift molded by deep Mediterranean outflow. *Geology*, **12**, 296–300.
- Faugères, J.C. and Stow, D.A.V.** (2008) Contourite drifts: nature, evolution and controls. In: *Contourites* (Eds Rebesco, M. and Camerlenghi, A.), *Dev. Sedimentol.*, **60**, 257–288.
- Folk, R.L. and Ward, W.C.** (1957) Brazos River bar (Texas); a study in the significance of grain size parameters. *J. Sed. Res.*, **27**, 3–26.
- Fonnesu, M., Palermo, D., Galbiati, M., Marchesini, M., Bonamini, E. and Bendias, D.** (2020) A new world-class deep-water play-type deposited by the syndepositional interaction of turbidity flows and bottom currents: the giant Eocene Coral Field in northern Mozambique. *Mar. Petrol. Geol.*, **111**, 179–201.
- Fuhrmann, A., Kane, I.A., Clare, M.A., Ferguson, R.A., Schomacker, E., Bonamini, E. and Contreras, F.A.** (2020) Hybrid turbidite-drift channel complexes: an integrated multiscale model. *Geology*, **48**, 562–568.
- García, M., Hernández-Molina, F.J., Llave, E., Stow, D.A.V., León, R., Fernández-Puga, M.C., Del Río, V.D. and Somoza, L.** (2009) Contourite erosive features caused by the Mediterranean outflow water in the Gulf of Cadiz: quaternary tectonic and oceanographic implications. *Mar. Geol.*, **257**, 24–40.
- García, M., Llave, E., Hernández-Molina, F.J., Ercilla, G., Alonso, A., Lobo, F.J., Casas, D., Fernández-Salas, L.M. and Mena, A.** (2020) Interplay between tectonics, gravitational and bottom current processes in the upper and middle continental slope of the Gulf of Cadiz. *Mar. Petrol. Geol.*, **121**, 104595.
- Giresse, P. and Wiewióra, A.** (2001) Stratigraphic condensed deposition and diagenetic evolution of green clay minerals in deep water sediments on the Ivory Coast-Ghana Ridge. *Mar. Geol.*, **179**, 51–70.
- Giresse, P.** (2008) Some aspects of diagenesis in contourites. In: *Contourites* (Eds Rebesco, M. and Camerlenghi, A.), *Dev. Sedimentol.*, **60**, 203–221.
- Gonthier, E.G., Faugères, J.C. and Stow, D.A.V.** (1984) Contourite facies of the Faro drift, Gulf of Cadiz. *Geol. Soc. Spec. Publ.*, **15**, 275–292.

- Gonthier, E., Faugères, J.C., Viana, A., Figueiredo, A. and Anschutz, P. (2003) Upper Quaternary deposits on the Sao Tomé deep-sea channel levee system (South Brazilian Basin): major turbidite versus contourite processes. *Mar. Geol.*, **199**, 159–180.
- Hammer, Ø., Harper, D.A. and Ryan, P.D. (2001) PAST: paleontological statistics software package for education and data analysis. *Palaeontol. Electron.*, **4**, 9.
- Hanebuth, T.J., Zhang, W., Hofmann, A.L., Löwemark, L.A. and Schwenk, T. (2015) Oceanic density fronts steering bottom-current induced sedimentation deduced from a 50 ka contourite-drift record and numerical modeling (off NW Spain). *Quatern. Sci. Rev.*, **112**, 207–225.
- Hanquiez, V., Mulder, T., Lecroart, P., Gonthier, E., Marchès, E. and Voisset, M. (2007) High resolution seafloor images in the Gulf of Cádiz, Iberian margin. *Mar. Geol.*, **246**, 42–59.
- Hebbeln, D., Van Rooij, D. and Wienberg, C. (2016) Good neighbours shaped by vigorous currents: cold-water coral mounds and contourites in the North Atlantic. *Mar. Geol.*, **378**, 171–185.
- Hesse, R. (1975) Turbiditic and non-turbiditic mudstone of Cretaceous flysch sections of the East Alps and other basins. *Sedimentology*, **22**, 387–416.
- Hernández-Molina, J., Llave, E., Somoza, L., Fernández-Puga, M.C., Maestro, A., León, R., Medialdea, T., Barnolas, A., García, M., Díaz del Río, V., Fernández-Salas, L.M., Vázquez, J.T., Lobo, F.J., Alverinho Dias, J.M., Rodero, J. and Gardner, J. (2003) Looking for clues to paleoceanographic imprints: a diagnosis of the gulf of Cadiz contourite depositional systems. *Geology*, **31**, 19–22.
- Hernández-Molina, F.J., Llave, E., Stow, D.A.V., García, M., Somoza, L., Vázquez, J.T., Lobo, F.J., Maestro, A., del Río, V.D., León, R. and Medialdea, T. (2006) The contourite depositional system of the Gulf of Cadiz: a sedimentary model related to the bottom current activity of the Mediterranean outflow water and its interaction with the continental margin. *Deep-Sea Res. Part II Topical Stud. Oceanogr.*, **53**, 1420–1463.
- Hernández-Molina, F.J., Stow, D.A.V., Alvarez-Zarikian, C. and Expedition 339 Scientists (2013) IODP Expedition 339 in the Gulf of Cadiz and off West Iberia: decoding the environmental significance of the Mediterranean outflow water and its global influence. IODP Expedition 339 in the Gulf of Cadiz and off West Iberia: decoding the environmental significance of the Mediterranean outflow water and its global influence. *Sci. Drilling*, **16**, 1–11.
- Hernández-Molina, F.J., Llave, E., Preu, B., Encilla, G., Fontan, A., Bruno, M., Serra, N., Gomiz, J.J., Brackenridge, R.E., Sierro, F.J., Stow, D.A.V., García, M., Juan, C., Sandoval, N. and Arnáiz, A. (2014) Contourite processes associated with the Mediterranean Outflow Water after its exit from the Strait of Gibraltar: global and conceptual implications. *Geology*, **42**, 227–230.
- Hernández-Molina, F.J., Sierro, F.J., Llave, E., Roque, C., Stow, D.A.V., Williams, T., Lofi, J., van der Schee, M., Arnáiz, A., Ledesma, S. and Rosales, C. (2016) Evolution of the gulf of Cadiz margin and southwest Portugal contourite depositional system: Tectonic, sedimentary and paleoceanographic implications from IODP expedition 339. *Mar. Geol.*, **377**, 7–39.
- Heezen, B.C., Ewing, M. and Ericson, D.B. (1954) Reconnaissance survey of the abyssal plain south of Newfoundland. *Deep-Sea Res.*, **2**, 122–133.
- Heezen, B.C., Tharp, M. and Ewing, M. (1959) The floors of the oceans: I. The North Atlantic. *Geol. Soc. Am.*, **65**, 1–115.
- Heezen, B.C. and Hollister, C.D. (1971) *The Face of the Deep*. Oxford Univ Press, New York, 650 pp.
- Hovikoski, J., Uchman, A., Weibel, R., Nøhr-Hansen, H., Sheldon, E., Ineson, J., Bjerager, M., Therkelsen, J., Olivarius, M., Larsen, M., Alsen, P. and Bojesen-Koefoed, J. (2020) Upper Cretaceous bottom current deposits, north-east Greenland. *Sedimentology*. <https://doi.org/10.1111/sed.12764>
- Hüneke, H., Hernández-Molina, F.J., Rodríguez-Tovar, F.J., Llave, E., Chiarella, D., Mena, A. and Stow, D.A.V. (2020) Diagnostic criteria based on microfacies for calcareous contourites, turbidites and pelagites in the Eocene-Miocene slope succession, southern Cyprus. *Sedimentology*. <https://doi.org/10.1111/sed.12792>
- Ito, M. (2002) Kuroshio current-influenced sandy contourites from the Plio-Pleistocene Kazusa forearc basin, Boso Peninsula, Japan. *Geol. Soc. London Mem.*, **22**, 421–432.
- Jiménez-Espejo, F.J., García Alix, A., Jiménez Moreno, G., Rodrigo Gámiz, M., Anderson, R.S., Rodríguez Tovar, F.J., Martínez Ruiz, F., Giralt, S., Delgado Huertas, A. and Pardo Igúzquiza, E. (2014) Saharan aeolian input and effective humidity variations over western Europe during the Holocene from high altitude record. *Chem. Geol.*, **374**, 1–12.
- Jung, M., Ilmberger, J., Mangini, A. and Emeis, K.C. (1997) Why some Mediterranean sapropels survived burn-down (and others did not). *Mar. Geol.*, **141**, 51–60.
- Kaboth, S., Bahr, A., Reichart, G.J., Jacobs, B. and Lourens, L.J. (2016) New insights into upper MOW variability over the last 150 kyr from IODP 339 Site U1386 in the Gulf of Cadiz. *Mar. Geol.*, **377**, 136–145.
- Kane, I.A., Clare, M.A., Miramontes, E., Wogelius, R., Rothwell, J.J., Garreau, P. and Pohl, F. (2020) Seafloor microplastic hotspots controlled by deep-sea circulation. *Science*, **368**, 1140–1145.
- Kenyon, N.H. and Belderson, R.H. (1973) Bedforms of the Mediterranean undercurrent observed with side-scan sonar. *Sed. Geol.*, **9**, 77–99.
- Laberg, J.S. and Camerlenghi, A. (2008) The significance of contourites for submarine slope stability. In: *Contourites* (Eds Rebescio, M. and Camerlenghi, A.), *Dev. Sedimentol.*, **60**, 537–556.
- Laskar, J., Robutel, P., Joutel, F., Gastineau, M., Correia, A.C.M. and Levrard, B. (2004) A long-term numerical solution for the insolation quantities of the Earth. *Astron. Astrophys.*, **428**, 261–285.
- Lebreiro, S.M., Antón, L., Reguera, M.I., Fernández, M., Conde, E., Barrado, A.I. and Yllera, A. (2015) Zooming into the Mediterranean outflow fossil moat during the 1.2–1.8 million years period (Early-Pleistocene)—an approach by radiogenic and stable isotopes. *Global Planet. Change*, **135**, 104–118.
- Lim, A., Huvenne, V.A.I., Vertino, A., Spezzaferri, S. and Wheeler, A.J. (2018) New insights on coral mound development from ground truthed high-resolution ROV mounted multibeam imaging. *Mar. Geol.*, **403**, 225–237.
- Llave, E., Hernández-Molina, F.J., Somoza, L., Díaz del Río, V., Stow, D.A.V., Maestro, A. and Alveirinho Dias, J.M. (2001) Seismic stacking pattern of the Faro-Albufeira contourite system (Gulf of Cadiz): a quaternary record of paleoceanographic and tectonic influences. *Mar. Geophys. Res.*, **22**, 475–496.
- Llave, E., Schönfeld, J., Hernández-Molina, F.J., Mulder, T., Somoza, L., Díaz del Río, V. and Sánchez-Almazo, I.

- (2006) High-resolution stratigraphy of the Mediterranean outflow contourite system in the Gulf of Cadiz during the late Pleistocene: the impact of Heinrich events. *Mar. Geol.*, **227**, 241–262.
- Llave, E., Hernández-Molina, F.J., Somoza, L., Stow, D.A.V. and Díaz del Río, V.** (2007) Quaternary evolution of the contourite depositional system in the Gulf of Cadiz. *Geol. Soc. London Spec. Publ.*, **276**, 49–79.
- Llave, E., Hernández-Molina, F.J., García, M., Ercilla, G., Roque, C., Juan, C., van Rooij, D., Rebesco, M., Brackenridge, R., Jané, G., Gómez-Ballesteros, M. and Stow, D.A.V.** (2019) Contourites along the Iberian continental margins: conceptual and economic implications. *Geol. Soc. Spec. Publ.*, **476**, 403–436.
- Lobo, F.J., Hernández-Molina, F.J., Somoza, L., Rodero, J., Maldonado, A. and Barnolas, A.** (2000) Patterns of bottom current flow deduced from dune asymmetries over the Gulf of Cadiz shelf (southwest Spain). *Mar. Geol.*, **164**, 91–117.
- Lobo, F.J., Maldonado, A. and Noormets, R.** (2010) Large-scale sediment bodies and superimposed bedforms on the continental shelf close to the Strait of Gibraltar: interplay of complex oceanographic conditions and physiographic constraints. *Earth Surf. Process. Landforms*, **35**, 663–679.
- Lofi, J., Voelker, A.H.L., Ducassou, E., Hernández-Molina, F.J., Sierro, F.J., Bahr, A., Galvani, A., Lourens, L.J., Pardo-Igúzquiza, E., Pezard, P. and Rodríguez-Tovar, F.J.** (2016) Quaternary chronostratigraphic framework and sedimentary processes for the Gulf of Cadiz and Portuguese Contourite Depositional Systems derived from Natural Gamma Ray records. *Mar. Geol.*, **377**, 40–57.
- Lovell, J.P.B. and Stow, D.A.V.** (1981) Identification of ancient sandy contourites. *Geology*, **9**, 347–349.
- Lowe, D.R.** (1979) Sediment gravity flows: their classification and some problems of application to natural flows and deposits. In: *Geology of Continental Slopes* (Eds Doyle, L.J. and Pilkey, O.H.), *SEPM Society for Sedimentary Geology*, **27**, 75–82.
- Lowe, D.R.** (1982) Sediment gravity flows; II, Depositional models with special reference to the deposits of high-density turbidity currents. *J. Sed. Res.*, **52**, 279–297.
- Lozano, P., Fernández-Salas, L.M., Hernández-Molina, F.J., Sánchez-Leal, R., Sánchez-Guillamón, O., Palomino, D. and Vázquez, J.T.** (2020) Multiprocess interaction shaping geoforms and controlling substrate types and benthic community distribution in the Gulf of Cádiz. *Mar. Geol.*, **423**, 106139.
- Lüdmann, T., Paulat, M., Betzler, C., Möbius, J., Lindhorst, S., Wunsch, M. and Eberli, G.P.** (2016) Carbonate mounds in the Santaren Channel, Bahamas: a current-dominated periplatform depositional regime. *Mar. Geol.*, **376**, 69–85.
- Maldonado, A., Somoza, L. and Pallarés, L.** (1999) The Betic orogen and the Iberian-African boundary in the Gulf of Cadiz: geological evolution (central North Atlantic). *Mar. Geol.*, **155**, 9–43.
- Martín-Chivelet, J., Fregenal-Martínez, M.A. and Chacón, B.** (2008) Traction structures in contourites. In: *Contourites* (Eds Rebesco, M. and Camerlenghi, A.), *Dev. Sedimentol.*, **60**, 157–182.
- Martins, L.R.** (2003) Recent sediments and grain-size analysis. *Gravel*, **1**, 90–105.
- McCave, I.N. and Tucholke, B.E.** (1986) Deep current-controlled sedimentation in the western North Atlantic. In: *The Geology of North America, The Western North Atlantic Region, Decade of North American Geology* (Eds Vogt, P.R. and Tucholke, B.E.), pp. 451–468. Geological Society of America, Boulder.
- McCave, I.N. and Hall, I.R.** (2002) Turbidity of waters over the Northwest Iberian continental margin. *Prog. Oceanogr.*, **52**, 299–313.
- McCave, I.N.** (2008) Size sorting during transport and deposition of fine sediments: sortable silt and flow speed. In: *Contourites* (Eds Rebesco, M. and Camerlenghi, A.), *Dev. Sedimentol.*, **60**, 121–142.
- Mestdagh, T., Lobo, F.J., Llave, E., Hernández-Molina, F.J., García Ledesma, A., Puga-Bernabéu, A., Fernández-Salas, L.M. and van Rooij, D.** (2020) Late Quaternary multi-genetic processes and products on the northern Gulf of Cadiz upper continental slope (SW Iberian Peninsula). *Mar. Geol.*, **427**, 106214.
- Middleton, G.V. and Hampton, M.A.** (1973) Sediment gravity flows: mechanics of flow and deposition. In: *Turbidity and Deep-Water Sedimentation* (Eds Middleton, G.V. and Bouma, A.H.), *SEPM, Pacific Section, Short Course Lecture Notes*, Anaheim, 1–38.
- Miramontes, E., Garziglia, S., Sultan, N., Jouet, G. and Cattaneo, A.** (2018) Morphological control of slope instability in contourites: a geotechnical approach. *Landslides*, **15**, 1085–1095.
- Miramontes, E., Eggenhuisen, J.T., Poneti, G., Silva Jacinto, R., Pohl, F. and Hernández-Molina, F.J.** (2020) Contour current-turbidity flow interaction from flume tank experiments: decoding processes and their morphological signatures. *Geology*, **48**, 353–357.
- Moreno, T., Querol, X., Castillo, S., Alastuey, A., Cuevas, E., Herrmann, L., Mounkaila, M., Elvira, J. and Gibbons, W.** (2006) Geochemical variations in aeolian mineral particles from the Sahara-Sahel Dust Corridor. *Chemosphere*, **65**, 261–270.
- Monteiro, P.M.S., Nelson, G., van der Plas, A., Mabilie, E., Bailey, G.W. and Klingelhoeffer, E.** (2005) Internal tidshelf topography interactions as a forcing factor governing the large-scale distribution and burial fluxes of particulate organic matter (POM) in the Benguela upwelling system. *Continental Shelf Res.*, **25**, 1864–1876.
- Mosher, D.C., Campbell, D.C., Gardner, J.V., Piper, D.J.W., Chaytor, J.D. and Rebesco, M.** (2017) The role of deep-water sedimentary processes in shaping a continental margin: The Northwest Atlantic. *Mar. Geol.*, **393**, 245–259.
- Mulder, T.** (2011) Gravity processes and deposits on continental slope, rise and abyssal plains. *Deep-Sea Sed.*, **63**, 25–148.
- Mulder, T., Hassan, R., Ducassou, E., Zaragosi, S., Gonthier, E., Hanquiez, V., Marchès, E. and Toucanne, S.** (2013) Contourites in the Gulf of Cadiz: a cautionary note on potentially ambiguous indicators of bottom current velocity. *Geo-Mar. Lett.*, **33**, 357–367.
- Nelson, C.H., Baraza, J. and Maldonado, A.** (1993) Mediterranean undercurrent sandy contourites, Gulf of Cadiz, Spain. *Sed. Geol.*, **82**, 103–131.
- Nelson, C.H., Baraza, J., Maldonado, A., Rodero, J., Escutia, C. and Barber Jr, J.H.** (1999) Influence of the Atlantic inflow and Mediterranean outflow currents on Late Quaternary sedimentary facies of the Gulf of Cadiz continental margin. *Mar. Geol.*, **155**, 99–129.
- Nieto-Moreno, V., Martínez-Ruiz, F., Giralte, S., Jiménez-Espejo, F.J., Gallego-Torres, D., Rodrigo-Gámiz, M., García-Orellana, J., Ortega-Huertas, M. and de Lange, G.J.**

- (2011) Tracking climate variability in the western Mediterranean during the Late Holocene: a multiproxy approach. *Clim. Past.*, **7**, 635–675.
- O'Brien, N.R., Nakazawa, K. and Tokuhashi, S. (1980) Use of clay fabric to distinguish turbiditic and hemipelagic siltstones and silts. In: *Deep-Water Turbidite Systems* (Ed. Stow, D.A.V.), *Sedimentology*, **27**, 47–61.
- Ochoa, J. and Bray, N.A. (1991) Water mass exchange in the Gulf of Cadiz. *Deep-Sea Res.*, **38**, S465–S503.
- Pettijohn, F.J. and Potter, P.E. (1964) *Atlas and Glossary of Primary Sedimentary Structures* (Eds Potter, P.E., Pettijohn, F.J. and Riggi, J.C.), Springer-Verlag, New York, 370 pp.
- Pickering, K.T. and Hiscott, R.N. (2015) *Deep marine Systems: Processes, Deposits, Environments, Tectonics and Sedimentation*. American Geophysical Union, John Wiley & Sons, 672 pp.
- Piper, D.J.W. (1972) Turbidite origin of some laminated mudstones. *Geol. Mag.*, **109**, 115–126.
- Piper, D.J.W. (1978) Turbidite, muds and silts on deep-sea fans and abyssal plains. In: *Sedimentation in Submarine Canyons, Fans and Trenches Dowden* (Eds Stanley, D.J. and Kelling, G.), pp. 163–176. Hutchinson and Ross, Stroudsburg, PA.
- Pomar, L., Morsilli, M., Hallock, P. and Bardenas, B. (2012) Internal waves, an under-explored source of turbulence events in the sedimentary record. *Earth Sci. Rev.*, **111**, 56–81.
- Preu, B., Hernández-Molina, F.J., Violante, R., Piola, A.R., Paterlini, C.M., Schwenk, T., Voig, I., Krastel, S. and Spiess, V. (2013) Morphosedimentary and hydrographic features of the northern Argentine margin: the interplay between erosive, depositional and gravitational processes and its conceptual implications. *Deep-Sea Res. Pt. I: Oceanographic Research Papers*, **75**, 157–174.
- Railsback, L.B., Gibbard, P.L., Head, M.J., Voarintsoa, N.R.G. and Toucanne, S. (2015) An optimized scheme of lettered marine isotope substages for the last 1.0 million years, and the climatostratigraphic nature of isotope stages and substages. *Quatern. Sci. Rev.*, **111**, 94–106.
- Rebesco, M., Hernández-Molina, F.J., van Rooij, D. and Wählin, A. (2014) Contourites and associated sediments controlled by deep-water circulation processes: state-of-the-art and future considerations. *Mar. Geol.*, **352**, 111–154.
- Rodero, J., Pallarés, L. and Maldonado, A. (1999) Late Quaternary seismic facies of the Gulf of Cadiz Spanish margin: depositional processes influenced by sea-level change and tectonic controls. *Mar. Geol.*, **155**, 131–156.
- Rodríguez-Tovar, F.J. and Hernández-Molina, F.J. (2018) Ichnological analysis of contourites: past, present and future. *Earth-Sci. Rev.*, **182**, 28–41.
- Rodríguez-Tovar, F.J., Hernández-Molina, F.J., Hüneke, H., Chiarella, D., Llave, E., Mena, A., Míguez-Salas, O., Dorador, J., de Castro, S. and Stow, D.A.V. (2019) Key evidence for distal turbiditic and bottom-current interactions from tubular turbidite infills. *Palaeogeogr. Palaeoclimatol. Palaeoecol.*, **533**, 109233.
- Rogerson, M. (2002) Climatic influence on sediment transport in the Mediterranean outflow current (Gulf of Cadiz, Spain). *Newsl. Micropalaeontol.*, **66**, 16–17.
- Rogerson, M., Rohling, E.J., Weaver, P.P.E. and Murray, J.W. (2005) Glacial to interglacial changes in the settling depth of the Mediterranean Outflow plume. *Paleoceanography*, **20**, PA3007.
- Rogerson, M., Rohling, E.J. and Weaver, P.P.E. (2006) Promotion of meridional overturning by Mediterranean-derived salt during the last deglaciation. *Paleoceanography*, **21**, PA4101.
- Rogerson, M., Rohling, E.J., Bigg, G.R. and Ramirez, J. (2012) Paleoceanography of the Atlantic-Mediterranean exchange: Overview and first quantitative assessment of climatic forcing. *Rev. Geophys.*, **50**, RG2003.
- Rothwell, R.G., Hoogakker, B., Thomson, J., Croudace, I.W. and Frenz, M. (2006) Turbidite emplacement on the southern Balearic Abyssal Plain (western Mediterranean Sea) during Marine Isotope Stages 1–3: an application of ITRAX XRF scanning of sediment cores to lithostratigraphic analysis. *Geol. Soc. London Spec. Publ.*, **267**, 79–98.
- Sánchez-Leal, R.F., Bellanco, M.J., Fernández-Salas, L.M., García-Lafuente, J., Gasser-Rubinac, M., González-Pola, C., Hernández-Molina, F.J., Pelegrí, J.L., Peliz, A., Relvas, P., Roque, D., Ruiz-Villarreal, M., Sammartino, S. and Sánchez-Garrido, J.C. (2017) The Mediterranean overflow in the Gulf of Cadiz: a rugged journey. *Sci. Adv.*, **3**, 1–11.
- Sansom, P. (2018) Hybrid turbidite–contourite systems of the Tanzanian margin. *Petrol. Geosci.*, **24**, 258–276.
- Scheuvs, D., Schütz, L., Kandler, K., Ebert, M. and Weinbruch, S. (2013) Bulk composition of northern African dust and its source sediments — a compilation. *Earth-Sci. Rev.*, **116**, 170–194.
- Schönfeld, J., Zahn, R. and de Abreu, L. (2003) Surface and deep-water response to rapid climate changes at the Western Iberian Margin. *Global Planet. Change*, **36**, 237–264.
- Schönfeld, J. and Zahn, R. (2000) Late Glacial to Holocene history of the Mediterranean outflow. Evidence from benthic foraminiferal assemblages and stable isotopes at the Portuguese margin. *Palaeogeogr. Palaeoclimatol. Palaeoecol.*, **159**, 85–111.
- Shanmugam, G. (2000) 50 years of the turbidite paradigm (1950s–1990s): deep-water processes and facies models—a critical perspective. *Mar. Pet. Geol.*, **17**, 285–342.
- Shanmugam, G., Spalding, T.D. and Rofheart, D.H. (1993a) Traction structures in deep-marine, bottom-current-reworked sands in the Pliocene and Pleistocene, Gulf of Mexico. *Geology*, **21**, 929–932.
- Shanmugam, G., Spalding, T.D. and Rofheart, D.H. (1993b) Process sedimentology and reservoir quality of deep-marine bottom-current reworked sands (sandy contourites): an example from the Gulf of Mexico. *AAPG Bull.*, **77**, 1241–1259.
- Shanmugam, G. (2002) Ten turbidite myths. *Earth-Sci. Rev.*, **58**, 311–341.
- Shanmugam, G. (2006) *Deep-Water Processes and Facies Models: Implications for Sandstone Petroleum Reservoirs*, Vol. 5 Amsterdam, the Netherlands: Elsevier Science.
- Shanmugam, G. (2012) *New perspectives on deep-water sandstones: origin, recognition, initiation, and reservoir quality. Handbook of Petroleum Exploration and Production*, **9**. Elsevier, Amsterdam, 524 pp. Available at: <https://www.elsevier.com/books/new-perspectives-on-deep-water-sandstones/shanmugam/978-0-444-56335-4>.
- Sierro, F.J., Flores, J.T. and Baraza, J. (1999) Late glacial to recent paleoenvironmental changes in the Gulf of Cadiz and formation of sandy contourite layers. *Mar. Geol.*, **155**, 157–172.
- Sierro, F.J., Hodell, D.A., Andersen, N., Azibeiro, L.A., Jiménez-Espejo, F.J., Bahr, A., Flores, J.A., Ausin, B., Rogerson, M., Lozano-Luz, R., Lebreiro, S. and Hernández-Molina, F.J. (2020) Mediterranean Overflow

- over the last 250 ky. Freshwater forcing from the tropics to the ice sheets. *Paleoceanogr. Paleoclimatol.*, **35**, e2020PA003931.
- Singh, A.D., Rai, A.K., Tiwari, M., Naidu, P.D., Verma, K., Chaturvedi, M., Niyogi, A. and Pandey, D.** (2015) Fluctuations of Mediterranean outflow water circulation in the Gulf of Cadiz during MIS 5 to 7: evidence from benthic foraminiferal assemblage and stable isotope records. *Global Planet. Change*, **133**, 125–140.
- Stow, D.A.V. and Lovell, J.P.B.** (1979) Contourites: their recognition in modern and ancient sediments. *Earth-Sci. Rev.*, **14**, 251–291.
- Stow, D.A.V.** (1982) Bottom currents and contourites in the North Atlantic. *Bull. Inst. Geol. Bassin Aquitaine*, **31**, 151–166.
- Stow, D.A.V. and Piper, D.J.W.** (1984) Deep-water fine-grained sediments: facies models. *Geol. Soc. London Spec. Publ.*, **15**, 611–646.
- Stow, D.A.V. and Shanmugam, G.** (1980) Sequence of structures in fine-grained turbidites: comparison of recent deep-sea and ancient flysch sediments. *Sed. Geol.*, **25**, 23–42.
- Stow, D.A.V. and Tabrez, A.R.** (1998) Hemipelagites: processes, facies and model. *Geol. Soc. London Spec. Publ.*, **129**, 317–337.
- Stow, D.A.V., Faugères, J.C., Viana, A. and Gonthier, E.** (1998) Fossil contourites: a critical review. *Sed. Geol.*, **115**, 3–31.
- Stow, D.A.V., Faugères, J.C., Howe, J.A., Pudsey, C.J. and Viana, A.R.** (2002) Bottom currents, contourites and deep-sea sediment drifts: current state-of-the-art. *Geo. Soc. London Mem.*, **22**, 7–20.
- Stow, D.A.V. and Faugères, J.C.** (2008) Contourite facies and the facies model. In: *Contourites* (Eds Rebesco, M. and Camerlenghi, A.), *Dev. Sedimentol.*, **60**, 223–250.
- Stow, D.A.V., Hunter, S., Wilkinson, D. and Hernández-Molina, F.J.** (2008) The nature of contourite deposition. In: *Contourites* (Eds Rebesco, M. and Camerlenghi, A.), *Dev. Sedimentol.*, **60**, 143–156.
- Stow, D.A.V., Hernández-Molina, F.J., Llave, E., Bruno, M., García, M., Díaz del Río, V., Somoza, L. and Brackenridge, R.E.** (2013a) The Cadiz Contourite Channel: sandy contourites, bedforms and dynamic current interaction. *Mar. Geol.*, **343**, 99–114.
- Stow, D.A.V., Hernández-Molina, F.J., Alvarez Zarikian, C.A. and Expedition 339 Scientists** (2013b) Proceedings IODP, 339. Integrated Ocean Drilling Program Management International, Tokyo.
- Stow, D.A.V. and Smillie, Z.** (2020) Distinguishing between deep-water sediment facies: turbidites, contourites and hemipelagites. *Geosciences*, **10**, 68.
- Takashimizu, Y., Kawamura, R., Rodríguez-Tovar, F.J., Dorador, J., Ducassou, E., Hernández-Molina, F.J., Stow, D.A.V. and Alvarez-Zarikian, C.A.** (2016) Reworked tsunami deposits by bottom currents: circumstantial evidences from Late Pleistocene to Early Holocene in the Gulf of Cádiz. *Mar. Geol.*, **377**, 95–109.
- Tallobre, C., Giresse, P., Bassetti, M.A., Loncke, L., Bayon, G., Buscail, R., Tudryn, A. and Zaragosi, S.** (2019) Formation and evolution of glauconite in the Demerara Contourite depositional system related to NADW circulation changes during late Quaternary (French Guiana). *J. S. Am. Earth Sci.*, **92**, 167–183.
- Thomson, J., Mercone, D., De Lange, G.J. and van Santvoort, P.J.M.** (1999) Review of recent advances in the interpretation of eastern Mediterranean sapropel S1 from geochemical evidence. *Mar. Geol.*, **153**, 77–89.
- Thomson, J., Crudeli, D., de Lange, G.J., Slomp, C.P., Erba, E., Corselli, C.T. and Calvert, S.E.** (2004) Florisphaera profunda and the origin and diagenesis of carbonate phases in eastern Mediterranean sapropel units. *Paleoceanography*, **19**, PA3003.
- Titschack, J., Thierens, M., Dorschel, B., Schulbert, C., Freiwald, A., Kano, A., Takashima, C., Kawagoe, N. and Li, X.** (2009) Carbonate budget of a cold-water coral mound (Challenger Mound, IODP Exp. 307). *Mar. Geol.*, **259**, 36–46.
- Tjallingii, R., Röhl, U., Kölling, M. and Bickert, T.** (2007) Influence of the water content on X-ray fluorescence core-scanning measurements in soft marine sediments. *Geochem. Geophys.*, **8**, Q02004.
- Toucanne, S., Mulder, T., Schönfeld, J., Hanquiez, V., Gonthier, E., Duprat, J., Cremer, M. and Zaragosi, S.** (2007) Contourites of the Gulf of Cadiz: a high-resolution record of the paleocirculation of the Mediterranean outflow water during the last 50,000 years. *Palaeogeogr. Palaeoclimatol. Palaeoecol.*, **246**, 354–366.
- van Dijk, J., Ziegler, M., de Nooijer, L.J., Reichart, G.J., Xuan, C., Ducassou, E., Bernasconi, S.M. and Lourens, L.J.** (2018) A saltier Glacial Mediterranean outflow. *Paleoceanogr. Paleoclimatol.*, **33**, 179–197.
- van den Berg, B.C., Sierro, F.J., Hilgen, F.J., Flecker, R., Larrasoana, J.C., Krijgsman, W., Flores, J.A. and Mata, M.P.** (2018) Imprint of Messinian salinity crisis events on the Spanish Atlantic margin. *Newsl. Stratigr.*, **51**, 93–115.
- Veldkamp, A. and Kroonenberg, S.B.** (1993) Application of bulk sand geochemistry in mineral exploration and Quaternary research: a methodological study of the Allier and Dore terrace sands, Limagne rift valley, France. *J. Appl. Geochem.*, **8**, 177–187.
- Viana, A.R. and Faugères, J.C.** (1998) Upper slope sand deposits: the example of Campos Basin, a latest Pleistocene-Holocene record of the interaction between along slope and down slope currents. In: *Geological Processes on Continental Margins: Sedimentation, Mass-Wasting and Stability* (Eds Stoker, M.S., Evans, D. and Cramp, A.), *Geol. Soc. Spec. Publ.*, **129**, 287–316.
- Viana, A.R., Faugères, J.C. and Stow, D.A.V.** (1998) Bottom-current-controlled sand deposits—a review of modern shallow-to deep-water environments. *Sed. Geol.*, **115**, 53–80.
- Vic, C., Garabato, A.C.N., Green, J.M., Waterhouse, A.F., Zhao, Z., Mélet, A., de Lavergne, C., Buijsman, M.C. and Stephenson, G.R.** (2019) Deep-ocean mixing driven by small-scale internal tides. *Nat. Commun.*, **10**, 1–9.
- Voelker, A.H., Lebreiro, S.M., Schönfeld, J., Cacho, I., Erlenkeuser, H. and Abrantes, F.** (2006) Mediterranean outflow strengthening during northern hemisphere coolings: a salt source for the glacial Atlantic? *Earth Planet. Sci. Lett.*, **245**, 39–55.
- Voelker, A.H., Salgueiro, E., Rodrigues, T., Jimenez-Espejo, F.J., Bahr, A., Alberto, A., Röhl, U., Loureiro, I., Padilha, M. and Rebotim, A.U.** (2015) Mediterranean outflow and surface water variability off southern Portugal during the early Pleistocene: a snapshot at Marine Isotope Stages 29 to 34 (1020–1135 ka). *Global Planet. Change*, **133**, 223–237.
- Wetzel, A. and Uchman, A.** (2012) Hemipelagic and Pelagic Basin Plains. In: *Trace Fossils as Indicators of Sedimentary Environments* (Eds Knaust, D. and Bromley, R.G.), *Dev. Sedimentol.*, **64**, 673–701.
- Wienberg, C. and Titschack, J.** (2017) Framework-forming scleractinian cold-water corals through space and time: a

- late Quaternary North Atlantic perspective. In: *Marine Animal Forests: the Ecology of Benthic Biodiversity Hotspots* (Eds Rossi, S., Bramanti, L., Gori, A. and Orejas Saco del Valle, C.), pp. 699–732. Springer, Cham.
- Wienberg, C., Titschack, J., Frank, N., de Pol-Holz, R., Fietzke, J., Eisele, M., Kremer, A. and Hebbeln, D. (2020) Deglacial upslope shift of NE Atlantic intermediate waters controlled slope erosion and cold-water coral mound formation (Porcupine Seabight, Irish margin). *Quat. Sci. Rev.*, **237**, 106310.
- Wold, S., Esbensen, K. and Geladi, P. (1987) Principal component analysis. *Chemom. Intell. Lab. Sys.*, **2**, 37–52.
- Wust, G. (1936) Schichtung und Zirkulation des Atlantischen Ozeans. Das Bodenwasser und die Stratosphäre. *Wiss. Erg. Dtsch. Atlant. «Meteor»*, 1925–1927, **6**, 1–288.
- Yu, X., Stow, D.A.V., Smillie, Z., Esentia, I., Brackenridge, R.E., Xie, X., Bankole, S., Ducassou, E. and Llave, E. (2020) Contourite porosity, grain size and reservoir characteristics. *Mar. Petrol. Geol.*, **117**, 104392.
- Ziegler, M., Jilbert, T., de Lange, G.J., Lourens, L.J. and Reichart, G.J. (2008) Bromine counts from XRF scanning as an estimate of the marine organic carbon content of sediment cores. *Geochem., Geophys.*, **9**, Q05009.
- Zou, H., Hastie, T. and Tibshirani, R. (2006) Sparse principal component analysis. *J. Comput. Graph. Stat.*, **15**, 265–286.

Manuscript received 18 June 2020; revision accepted 14 October 2020

Supporting Information

Additional information may be found in the online version of this article:

Table S1. Modal analysis data based on 300-point modal analysis in thin section from F1 to F5. Proportions of sediment components are re-normalized to total 100%.

Table S2. Principal Component Analysis (PCA) of integrated XRF-scan data and grain size: variable loadings for the three significant axes. Underlined bold: highest load of each variable in the corresponding axis. Mn is significant only for Axis 3. Variance explained: Axis 1 = 46.9%; Axis 2 = 12.8%; Axis 3 = 10.0% at Site U1388 and Axis 1 = 55.7%; Axis 2 = 11.3%; Axis 3 = 8.1% at Site U1389.

Table S3. Sites, coordinates, water depth, analyses and corresponding water mass of sites used for comparison in Fig. 18.